



Publication Year	2020
Acceptance in OA @INAF	2021-08-27T10:34:06Z
Title	Testing Comptonization as the Origin of the Continuum in Nonmagnetic Cataclysmic Variables: The Photon Index of X-Ray Emission
Authors	Maiolino, T; Titarchuk, L; D'Amico, F; Cheng, ZQ; Wang, W; et al.
DOI	10.3847/1538-4357/abab93
Handle	http://hdl.handle.net/20.500.12386/30984
Journal	THE ASTROPHYSICAL JOURNAL
Number	900

Testing Comptonization as the origin of the continuum in nonmagnetic Cataclysmic Variables. The photon index of X-ray emission

T. MAIOLINO,^{1,2,3} L. TITARCHUK,^{3,4} F. D'AMICO,⁵ Z. Q. CHENG,^{1,2} W. WANG,^{1,2} M. ORLANDINI,⁶
AND FILIPPO FRONTERA^{3,6,7}

¹*School of Physics and Technology, Wuhan University, Wuhan 430072, China*

²*WHU-NAOC Joint Center for Astronomy, Wuhan University, Wuhan 430072, China*

³*Dipartimento di Fisica, Università di Ferrara, via Saragat 1, 44122 Ferrara, Italy*

⁴*Astro Space Center, Lebedev Physical Institute, Russian Academy of Sciences, Profsovznav ul. 84/32, Moscow 117997, Russia*

⁵*Instituto Nacional de Pesquisas Espaciais, Avenida dos Astronautas 178, 12227-010 S.J. dos Campos-SP, Brazil*

⁶*INAF/OAS Bologna, via Gobetti 101, 40129 Bologna, Italy*

⁷*ICRANET Piazzale d. Repubblica 10-12, 65122 Pescara (PE), Italy*

ABSTRACT

X-ray spectra of nonmagnetic cataclysmic variables (nmCVs) in the ~ 0.3 – 15 keV energy band have been described either by one or several optically thin thermal plasma components, or by cooling flow models. We tested if the spectral continuum in nmCVs could be successfully described by Comptonization of soft photons off hot electrons presented in a cloud surrounding the source [the transition layer, (TL)]. We used publicly *XMM-Newton* Epic-pn, *Chandra* HETG/ACIS and LETG/HRC, and *RXTE* PCA and HEXTE observations of four Dwarf Novae (U Gem, SS Cyg, VW Hyi and SS Aur) observed in the quiescence and outburst states. In total, we analyzed 18 observations, including a simultaneous 0.4–150 keV *Chandra/RXTE* spectrum of SS Cyg in quiescence. We fitted the spectral continuum with up to two thermal Comptonization components (COMPTT or COMPTB models in XSPEC), using only one thermal plasma temperature and one optical depth. In this framework the two seed photon components are coming presumably from the innermost and outer parts of the TL (or innermost part of the disk). We obtained that the thermal Comptonization can successfully describe the spectral continuum of these nmCV in the ~ 0.4 – 150 keV energy band. Moreover, we present the first principal radiative transfer model which explains the quasi-constancy of the spectral photon index observed around 1.8, which strongly supports the Comptonization framework in nmCVs.

Keywords: -rays: binaries — cataclysmic variables — accretion, radiation mechanisms: thermal – scattering

1. INTRODUCTION

The power source of X-rays in cataclysmic variables (CVs) is known to be due to the accretion of matter onto a compact object – a white dwarf (WD). In non-magnetic CVs (nmCVs), as well as in all CVs containing accretion disks, the accretion disk is generally too cold ($kT \ll 1$ keV) to emit X-rays (Lewin & van der Klis 2006). The major source of X-rays have been identified with the transition layer (TL) – the region between the spiralling accretion disk and the surface of a more slowly rotating WD, wherein half of the gravitational energy is expected to be released. Physical characteristics of the TL and the system have been described to account for both the observed soft and hard X-ray spectral emission (Pringle & Savonije 1979; Patterson & Raymond 1985a,b; Titarchuk et al. 2014).

In the standard TL framework the accretion rate determines the TL optical depth, which along with the electron temperature T_e of the TL drive the X-ray spectral emission. Patterson & Raymond (1985a, and references therein) suggested that at high accretion rate ($\dot{M} \gtrsim 10^{16}$ g s⁻¹), the TL is expected to be optically thick and to radiate a blackbody component at $T \sim 10^5$ K. On the contrary, at low accretion rate ($\dot{M} < 10^{16}$ g s⁻¹) – i.e., in the quiescent state – the TL is expected to have a lower density and to be optically thin. Because optically thin plasma does not cool efficiently, higher temperatures are expected in this state. The cooling of the TL in this case has been described by a thermal bremsstrahlung component, emitting hard X-rays at temperature $T \sim 10^8$ K (Patterson & Raymond 1985b). Part (up to a half) of the hard X-rays emitted by the TL must be absorbed by a WD surface, and reradiated in soft X-rays with an effective temperature $T_{eff} \lesssim 10^{5-6}$ K (see, e.g., Patterson & Raymond 1985b; Williams et al. 1987; Mukai 2017).

Early spectral analysis of nmCVs showed that their spectral continuum were generally well described by only one thermal bremsstrahlung component, i.e., by a single plasma temperature in the 1-5 keV energy range, and of a few keV up to ~ 10 keV in the case of dwarf novae (Lewin & van der Klis 2006, and references therein).

In the last decades the single temperature MEKAL (or its variation VMEKAL) model (see XSPEC; Mewe et al. 1986; Liedahl et al. 1995) has been broadly used to fit the CVs spectra. In this model the X-ray radiation is produced by a hot, optically-thin thermal plasma: the basis of the continuum radiation is free-free (bremsstrahlung), free-bound, and two-photon emission. The emission lines observed are included into this model and are modeled by: excitation from electron impact, radiative and dielectronic recombination and by inner-shell excitation and ionization. As the model is in the optically thin limit, photo-ionization or photo-excitation effects are not taken into account. Similar to the MEKAL model, the APEC code¹ (or its variations VAPEC and VVAPEC) is another thermal optically thin plasma model which has been commonly used to describe the spectra of nmCVs.

Spectral analysis using data from X-ray observatories with better signal-to-noise and energy resolution (e.g., *XMM-Newton* and *SUZAKU*) showed that only one optically thin plasma temperature does not satisfactory fit the spectra of all sources (Lewin & van der Klis 2006) – there are analyses in which two or even more plasma temperatures are needed to obtain good spectral fits (see, e.g., Pandel et al. 2003). For that reason, it has been suggested that the cooling flow spectral model should represent a more physically correct description of the observed X-ray spectra.

The gas flow in cooling flow models is assumed to be composed by a range of temperatures which vary from the hot shock temperature kT_{max} (the maximal temperature to that the plasma is heated up; $kT_{max} \sim 10 - 80$ keV) to the temperature when the optically thin cooling material settles on to

¹ Calculated using the ATOMDB code, more information can be found at <http://atomdb.org>.

the WD surface (see Mukai et al. 2003; Byckling et al. 2010, and references therein). Cooling flow models are available in XSPEC, as: CEMEKL or CEVMKL, MKCFLOW or VMCFLOW (Mushotzky & Szymkowiak 1988) – these models were originally developed to describe the cooling flows in clusters of galaxies. It is now known that such models do not successfully describe these sources (as stated in Mukai et al. 2003). All of them basically use an optically thin thermal plasma model for the individual temperature components.

Baskill et al. (2005) used the CEMEKL cooling flow model to successfully fit ~ 30 DNe spectra observed with *ASCA* (their source sample includes three out of four of the nmCVs analyzed in this paper: SS Cyg, U Gem and VW Hyi). Byckling et al. (2010) through *XMM-Newton*, *Suzaku* and *ASCA* data, fitted the spectra of 12 DNe (their source sample includes SS Cyg, U Gem and SS Aur) using either one temperature optically thin plasma model or a cooling flow model. All fits include spectral components taking into account absorption created by the presence of material along the line of sight. A photoelectric absorption column is usually used (e.g., the WABS model in XSPEC was extensively used in the last years), with additional partial covering absorption (e.g., PCFABS in XSPEC) in some cases – to take into account for the presence of an intrinsic absorber located somewhere within the binary system (see, e.g., Byckling et al. 2010).

Mukai et al. (2003), using *Chandra* high energy transmission grating (HETG) data, stated that there are two types of CV X-ray spectra and suggested that the spectral differences might lie on the specific accretion rate (accretion rate per unit of area) of the systems. They showed that all three nmCVs analyzed (and an unusual Intermediate Polar (IP), EX Hya) had their spectra better described by cooling flow models, whereas other sources analyzed (which were all of the IP type) had their spectra better described by the photo-ionization model (PHOTOION model in XSPEC).

Figure 1 shows the spectral components of the nmCV SS Cyg in the 0.2–40 keV energy band (Ishida et al. 2009). This picture is proposed by Done & Osborne (1997) on the basis of their analysis of SS Cyg using *Ginga* and *ASCA* data, and represents a general framework of the radiative process in CVs, widely accepted (by the time of this paper) by the scientific community. The red line in Figure 1 represents the hard X-ray spectrum – primarily composed of an optically thin thermal plasma emission with a temperature distribution. In this framework, a part of the hard X-rays produced in the optically thin thermal plasma suffers reflection from the the accretion disk and/or the white dwarf surface, which represent a significant fraction of the observed X-ray flux. This reflected component (represented by *green* line in Figure 1) explains, in the same way as in low mass X-ray binaries (LMXBs) and type I Seyfert galaxies (George & Fabian 1991), the production of the neutral fluorescent iron K_α line observed at 6.4 keV in several CVs. The presence of this feature is explained by reflection of X-rays from the accretion disk and/or the WD surface, where relatively cold iron with temperatures $\leq 10^6 K$ is present. In general, up to three distinct iron emission lines in the ~ 6.4 to 7.0 keV energy range may be present, in the spectra of CVs, related to neutral, He-like and H-like k_α Fe lines. The He-like and H-like lines (at ~ 6.7 and 7.0 keV, respectively) are produced by a plasma with relatively higher temperatures of 10^{7-8} K (see, e.g. Rana et al. 2006).

For a more detailed review on nmCVs and their X-ray emission – as well as on other types of CVs – see for example Warner (1995) and Mukai (2017).

The Comptonization model is not one of the standard models which has been currently used to describe the CV continuum. However, CVs, mainly the non-magnetic and IP types, share structural similarities with LMXBs – i.e., these systems contain: an accretion disk (which appears either entirely

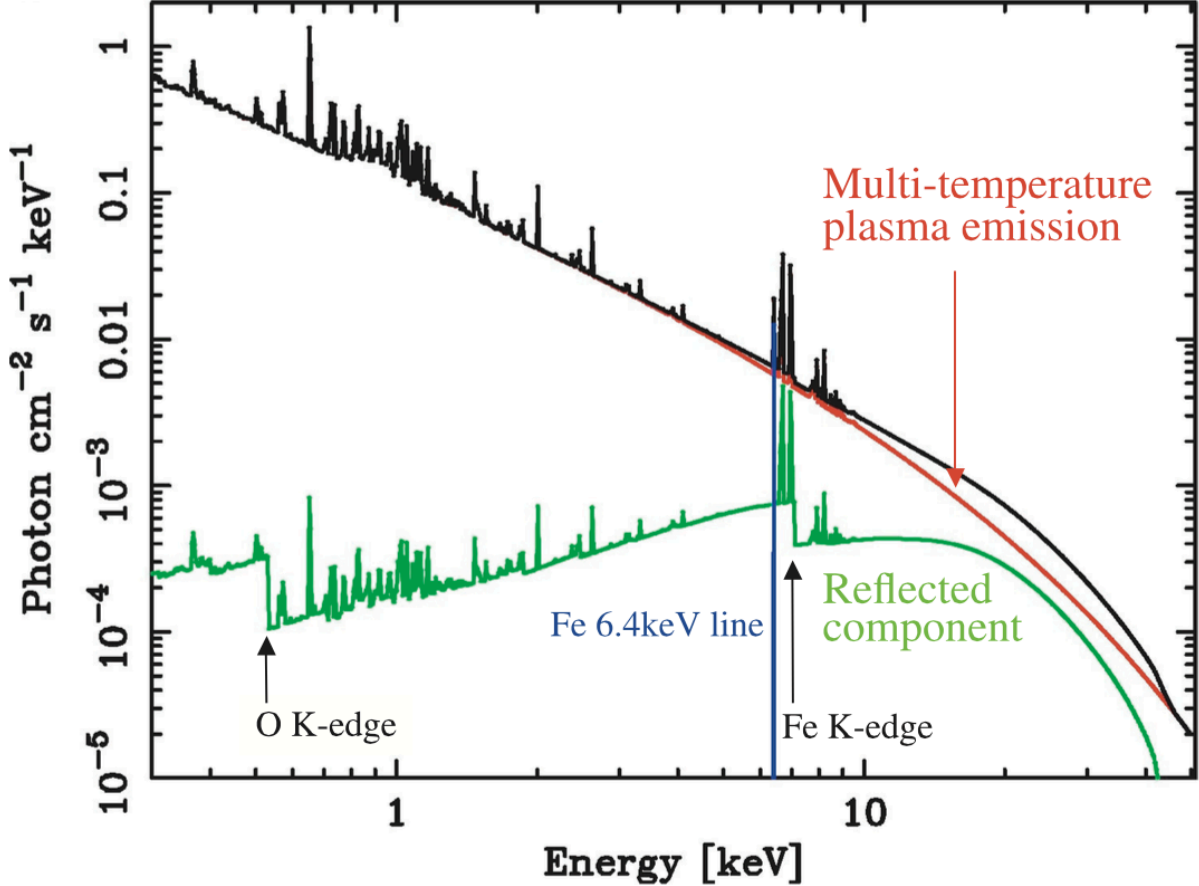


Figure 1. The spectral components of SS Cyg in the 0.2–40 keV band, which basically represents the spectral modeling of CVs: a multi-temperature optically thin thermal plasma represents the hard X-ray emission (red), the reflection of the hard X-rays by the accretion disc or/and the surface of the WD produces the fluorescent iron K_{α} lines observed and a hump in the continuum (green) (Done & Osborne 1997; Ishida et al. 2009).

in nmCVs or partially in IPs), a transition layer (TL, corona), and a compact object. Taking into account these geometric/structural similarities and the radiative processes used to describe the continuum of LMXBs – which has changed from bremsstrahlung to the Comptonization – we tested if the spectral continuum of nmCVs and IPs could be successfully described by the Comptonization (up-scattering) of soft photons off hot electrons of a Compton cloud around the compact object, as it is in LMXBs. In this paper we present the results of this verification performed on nmCVs. We used 4 *XMM-Newton* Epic-pn, 8 *Chandra* (LETG/HRC and HETG/ACIS), and 6 *RXTE* (PCA and HEXTE) publicly observations of four Dwarf Novae (DNe): U Gem, SS Cyg, VW Hyi and SS Aur. These sources were observed only in quiescence by *XMM-Newton*, and in the quiescence and outburst states by *Chandra* and *RXTE*. In our observational sample, we have a simultaneous *Chandra/RXTE* observation of SS Cyg, which provides us the 0.4–150 keV broadband spectral description of this source in the quiescence state.

In a previous paper by Titarchuk et al. (2014), the authors found that the photon index, Γ in the NS sources strongly concentrated at 2. Moreover, they analytically demonstrated, using the radiative

transfer model, that this is a result of the gravitational release of accreted material in the transition layer (TL) near a NS surface. Our goal is to show that the similar effect should be seen in WDs in which we should take into account an absorption of the X-ray radiation by the WD surface (while in a NS, its surface reflects X-ray radiation).

This paper is organized as follows: in section 2 we describe our source sample, in section 3 we present the data reduction of the *XMM-Newton* (Epic-pn), *Chandra* (LETG/HRC and HETG/ACIS), and *RXTE* (PCA and HEXTE) observations, in section 4 we describe the spectral analysis, in section 5, we present our radiative transfer model which explains the invariance of the photon index, in section 6 we discuss the results of the paper, and in section 7 we present our final conclusions.

2. SOURCE SAMPLE

Since the goal of this work is to study the spectral continuum of nmCVs, any source belonging to this type have been included in our sample. Because we have started this study using XMM-Newton Epic-pn data, we have chosen sources present in the archive with publicly Epic-pn observations. Thus we included 4 nmCVs in our sample: U Gem, SS Cyg, VW Hyi and SS Aur, which are amongst the brightest X-ray nmCV.

For completeness, in this section we give a brief description of these sources. We present the binary system parameters [orbital period (P_{orb}), rotational period (P_{spin}), and an inclination angle (i)], distance, and temporal properties, and examples of the spectral modeling published in the literature for each source.

2.1. *U Gem*

U Gem has a WD with mass (M_{WD}) of $1.07 \pm 0.08 M_{\odot}$ (Ritter & Kolb 2003). It appears to be at most slowly rotating ($v \sin i \lesssim 100 \text{ km s}^{-1}$), which corresponds to 20% of the break-up velocity (Lewin & van der Klis 2006). The secondary star has a mass M_2 of $0.39 \pm 0.02 M_{\odot}$ (Ritter & Kolb 2003) and spectral type M4 V (Harrison et al. 2000). The system is located at $100 \pm 4 \text{ pc}$ of distance; it has an orbital period of 4.246 h (Harrison et al. 2004) and an inclination i of $69 \pm 2^{\circ}$ (Ritter & Kolb 2003). Dips in the X-ray light curves have been observed during quiescence (Szkody et al. 1996, 2002), and during normal (Long et al. 1996) and anomalously outbursts (of ~ 45 days) (Mason et al. 1988) as well. The X-ray dips in U Gem are less deep in quiescence than in outburst. The morphology of the dips changes from cycle to cycle, related to changes in the absorbing material. In U Gem both soft and hard X-ray fluxes are higher during outburst than in quiescence by a factor of ~ 10 – 100 (see Lewin & van der Klis 2006, and references therein).

Güver et al. (2006) studied the spectral emission of U Gem in both quiescence and outburst states, using the same *XMM-Newton*, *Chandra* HETG/ACIS, and *RXTE* PCA observations present in our sample. They fitted the quiescence spectra with both CEMEKL (or CVMKL) and MKCFLOW cooling flow models, finding a maximal temperature kT_{max} in the $\sim 15 - 38 \text{ keV}$ range. They report, for the first time, properties of the hard X-ray emission of this source in outburst. In this state, an extra X-ray non-thermal component is needed, in addition to a simple mekal-based multi-temperature component, to obtain an acceptable spectral fit. Though deviations from the continuum are still noticeable, this extra component was better described by a power law rather than other models (such as thermal bremsstrahlung, see Table 4 and Fig. 3 and 4 therein). The authors report $kT_{\text{max}} = 9.49 \pm 4.1 \text{ keV}$ and $18.44 \pm 10.5 \text{ keV}$ for the CEMEKL component in the *Chandra* HETG/ACIS HEG and MEG spectra, respectively; and a power-law component with photon index Γ of 0.54 ± 0.16

and 0.64 ± 0.06 , respectively. Analyzing the 3-20 keV PCA spectra throughout the 2004 outburst the authors demonstrated evidence of a transient hard X-ray component – since in 9 out of 23 spectra the power-law component was not required. They suggested that this component is driven by a mechanism temporarily present during outburst, which could be either reflection of X-ray coming from either the optically thick plasma or from an optically thick boundary layer, as well from a transient magnetosphere present during outburst (see Güver et al. 2006, and reference therein). On the other hand, they noticed that spectral features expected by the reflection scenario such as the K_α fluorescent lines are either very weak or not observed during the outburst state in U Gem. It is important to stress, however, that reflection scenario is not the only one capable to explain the K_α fluorescent line production (see, e.g., Maiolino et al. 2019).

Mukai et al. (2003) showed that the *Chandra* spectrum of the DN U Gem (as well as SS Cyg and V603 Aql) can be described by the multi-temperature bremsstrahlung cooling-flow model MKCFLOW with $kT_{\max} = 20$ keV. Byckling et al. (2010) fitted the *XMM-Newton* U Gem spectrum in quiescence also using the MKCFLOW model and found a maximum temperature $kT_{\max} = 25.82_{-1.43}^{+1.98}$ keV and an equivalent width of the Fe 6.4 keV line (EW6.4) of 60_{-32}^{+33} eV. Using, on the other hand, a single temperature optically thin plasma model (MEKAL) they found $kT = 0.78_{-0.01}^{+0.03}$ keV and EW6.4 of 50_{-24}^{+25} eV. Xu et al. (2016) analyzed the spectra of 41 CVs observed with *Suzaku*. They used the single temperature model APEC to fit the 2–10 keV continuum and 3 Gaussian components (at 6.4 keV, 6.7 keV, and 7.0 keV) to fit the Fe emission lines of U Gem in quiescence. They found a plasma temperature $kT = 16.5_{-3.31}^{+4.49}$ keV; and EW 6.4 = 43_{-11}^{+16} eV, EW6.7 = 258_{-21}^{+22} eV, and EW 7.0 = 178_{-11}^{+11} eV.

2.2. SS Cyg

SS Cyg belongs to the U Gem type of DN. The system has a WD with mass M_{WD} of $1.19 \pm 0.02 M_\odot$, a secondary star with mass M_2 of $0.704 \pm 0.002 M_\odot$ (Friend et al. 1990) and K5/5 spectral type (Ritter & Kolb 2003). The binary system is located at 166 ± 12 pc (Harrison et al. 1999, 2004), has an inclination angle i of $37 \pm 5^\circ$ (Ritter & Kolb 2003) and a period of 6.603 h (Harrison et al. 2004). This source is one of the DNe broadly studied in outbursts, as it shows an optical outburst every ~ 50 days, in which m_V changes from 12th to 8th magnitude (Mauche & Robinson 2001; Lewin & van der Klis 2006, see for example, Figure 10.1 therein). They claim that the system shows a reflection component in the quiescence and outburst states, with larger contribution in the outburst (Done & Osborne 1997; Lewin & van der Klis 2006, and references therein). Mukai et al. (2003) found a maximum plasma temperature kT_{\max} of 80 keV using fits of the *Chandra* spectrum of this source in quiescence and the multi-temperature MKCFLOW model.

Okada et al. (2008) analyzed the two *Chandra*/HETG observations present in our sample. They constrained the power law index and the temperature of the boundary layer in the framework of the CEMEKL model.

Ishida et al. (2009) presented a *Suzaku* XIS and HXD-PIN analysis of this source observed, in November 2005, in the quiescence and outburst states. Using the multi-temperature thin plasma model CVMEKAL (model in XSPEC), they found a maximum temperature of the plasma kT_{\max} of $20.4_{-2.6}^{+4.0}$ (stat) ± 3.0 (sys) keV in quiescence, and of $6.0_{-0.2}^{+1.3}$ keV in outburst.

Byckling et al. (2010) fitted a *SUZAKU* XIS spectrum of SS Cyg in quiescence using the optically thin plasma model MEKAL and the cooling model MKCFLOW (including photoelectric absorption and partial covering as well). As a result they obtained a plasma temperature of $10.44_{-0.17}^{+0.16}$ keV and

a maximum temperature of the plasma kT_{\max} of $41.99_{-0.76}^{+1.20}$ keV, respectively. In their fits EW6.4 is equal to 75_{-4}^{+9} eV and 73_{-7}^{+6} eV, respectively. Xu et al. (2016), using *Suzaku* data (during an outburst) and the single temperature model APEC, fit the 2–10 keV continuum including 3 Gaussian components of the iron emission lines, (at 6.4 keV, 6.7 keV, and 7.0 keV). As a result they estimated a plasma temperature $kT = 8.15_{-0.91}^{+1.23}$ keV; and EW6.4 = 67_{-10}^{+11} eV, EW6.7 = 415_{-30}^{+41} eV, and EW7.0 = 48_{-11}^{+15} eV.

2.3. VW Hyi

VW Hyi is a well-studied source. It is located at 54 ± 0.1 pc (see Nakaniwa et al. 2019, and references therein) and belongs to the SU UMa sub-group of DNe (Warner 1987), which undergoes both normal DN outbursts and super-outbursts (Godon & Sion 2005). The M_{WD} was estimated as $0.63 \pm 0.15 M_{\odot}$ (Schoembs & Vogt 1981)². The secondary star has a mass M_2 of $0.11 \pm 0.02 M_{\odot}$ (Schoembs & Vogt 1981) and it is a M6V star (Godon & Sion 2005). The binary system has an inclination angle i of $60 \pm 10^{\circ}$ (Schoembs & Vogt 1981), and an orbital period of 0.074271 days (~ 1.783 h, which lies below the CV period gap; Ritter & Kolb 2003). VW Hyi shows super-humps (which are variations in the light curves at a period of a few per cent longer than the orbital period) with a period of 0.07714 days (~ 1.85 h). VW Hyi lies along a line of sight with a very low interstellar absorption, $N_H \approx 6 \times 10^{17}$ atoms cm^{-2} (Polidan et al. 1990). This low interstellar absorption allows us to observe this system in almost all wavelength ranges.

The source shows a very low mass accretion rate during quiescence, $\dot{M} \approx 10^{-11} M_{\odot} \text{ yr}^{-1}$, emitting significantly in UV (between 35–47%; see Godon & Sion 2005, and references therein). The first X-ray observations of VW Hyi in quiescence were done in 1984 with *EXOSAT* (van der Woerd & Heise 1987), in which persistent hard (1–6 keV) and soft (0.04–1.5 keV) X-ray fluxes were observed. In the spectral analysis, an equally best fit was pointed out either using a power-law or a thermal bremsstrahlung model ($kT > 5$ keV) without interstellar absorption ($N_H < 10^{21}$ atoms cm^{-2}).

Belloni et al. (1991) fitted the spectrum of VW Hyi observed in quiescence by *ROSAT* using the optically-thin thermal plasma model Raymond-Smith with a single temperature (Raymond & Smith 1977). They found a temperature of 2.17 ± 0.15 keV for zero interstellar absorption (when absorption was included and significantly different temperature and flux were not found). Hasenkopf & Eracleous (2002) analyzed the spectrum of VW Hyi observed with *ASCA*, and using two- and multiple temperature thermal plasma models revealed that the resulting temperatures lie mostly between 4 and 10 keV.

Pandel et al. (2003, 2005) analyzed a *XMM-Newton/EPIC* spectrum of VW Hyi in quiescence (the same observation analyzed in this paper). They modeled the spectrum with cooling flow models – i.e., with multi-temperature thin thermal plasma models (CEMEKL, CEVMKL and MKCFLOW) – and obtained a maximum temperature kT_{\max} between 6 and 8 keV. Pandel et al. (2003) attempted to fit the EPIC spectra with one or two single-temperature MEKAL components (as commonly used to fit DNe spectra), but obtained a satisfactory fit only when three components of their model were used.

Nakaniwa et al. (2019) have also analysed the same *XMM-Newton/EPIC* observation present in our sample along with 3 more *SUZAKU/XIS* observations in quiescence. They report that all 0.2–10 keV spectra are moderately well fitted by the CEVMKL and VMCFLOW cooling flow models, with a maximal temperature of 5–9 keV. Namely, for the *XMM-Newton* observation, they obtained

² A gravitational redshift determination done by Sion et al. (1997) yielded $M_{WD} = 0.86_{-0.32}^{+0.18} M_{\odot}$

a plasma temperature kT_{\max} of $5.32_{-0.22}^{+0.23}$ keV and $6.95_{-0.19}^{+0.20}$ keV with the CEVMKL and VMCFLOW models, respectively.

Xu et al. (2016), using *Suzaku* data and the single temperature model APEC to analyze the 2–10 keV continuum, and 3 Gaussian components (at 6.4 keV, 6.7 keV, and 7.0 keV) fit the Fe emission lines, found in VW Hyi (in the quiescence state). They found a plasma temperature kT of $5.79_{-2.14}^{+4.71}$ keV; and for the emission Fe lines they estimated $\text{EW}_{6.4} = 0.01$ eV (upper limit), $\text{EW}_{6.7} = 1392_{-172}^{+152}$ eV, and $\text{EW}_{7.0} = 42_{-42}^{+58}$ eV.

2.4. *SS Aur*

SS Aur belongs to the U Gem type of DNe with high mass accretion rates \dot{M} . The binary system is located at 167_{-09}^{+10} pc (Harrison et al. 2004) and has an inclination angle i of $38 \pm 16^\circ$. The system has an orbital period of 0.1828(1) days (which is equivalent to 4.387 h) (Shafter & Harkness 1986; Byckling et al. 2010; Harrison et al. 2004). The system hosts a WD with a mass M_{WD} of $1.08 \pm 0.40 M_\odot$, and a secondary star of \sim M1 V type (Harrison et al. 2000) with a mass M_2 of $0.39 \pm 0.02 M_\odot$ (Ritter & Kolb 2003, and references therein). Byckling et al. (2010) fitted a *SUZAKU* XIS spectrum of SS Aur in quiescence using both the optically thin plasma model MEKAL and the cooling model MKCFLOW (including photoelectric absorption and partial covering as well). They obtained a plasma temperature of 6.35 ± 0.40 keV and a maximum temperature of the plasma kT_{\max} of $23.47_{-3.02}^{+4.01}$ keV, respectively. In these fittings $\text{EW}_{6.4}$ is equal to 73_{-36}^{+37} eV and 86_{-53}^{+52} eV, respectively. Xu et al. (2016), using *Suzaku* data and the single temperature model APEC in the 2–10 keV continuum and 3 Gaussian (the Fe emission lines) components (at 6.4 keV, 6.7 keV, and 7.0 keV) found that SS Aur, in the quiescence state, has the best fit parameters of a plasma temperature of $8.48_{-2.61}^{+5.34}$ keV; and $\text{EW}_{6.4} = 47_{-29}^{+60}$ eV, $\text{EW}_{6.7} = 325_{-65}^{+90}$ eV, and $\text{EW}_{7.0} = 169_{-49}^{+57}$ eV.

3. DATA REDUCTION

XMM-NEWTON

We analyzed in total four *XMM-Newton* EPIC-pn public observations, one observation of each source. See Table 1 for a log of the observations. All *XMM-Newton* observations were taken with the sources in the quiescence state.

VW Hyi, U Gem and SS Aur were observed with the pn camera operating in Imaging mode, while SS Cyg was observed with the pn camera in Timing mode. All light curves and spectra were extracted through the Science Analysis Software (SAS) version 14.0.0. We strictly followed the recommendations for the pn camera in each mode of observation (timing and imaging, respectively). Following Guainazzi (2016), we considered the 0.3–15.0 keV spectral energy range for observations taken in Imaging mode, and the 0.7–10.0 keV range for the observation taken in Timing mode.

We checked spectral variability extracting two light curves for each source. The two light curve energy ranges were selected accordingly to the observational mode: from 0.3 to 4.0 keV and 4.0 to 15 keV for observations taken in Imaging mode; and from 0.7 to 4.0 keV and 4.0 to 10.0 keV for observation taken in Timing mode. We computed ratios between the light curves in the two energy bands (hardness ratio, HR). The HR of SS Aur showed a time interval of increased noise in the end of the exposure, which was discarded in the spectral extraction. For all other observations, a count rate variability was not associated with a significant change in the HR or with noise increase. We used therefore the total EPIC-pn exposure time in the spectral extraction of these observations.

Table 1. Log of the *XMM-Newton*, *Chandra* and *RXTE* observations

Source	Observatory	Instrument	Obs. ID	Start Time Date (UTC)	End Time Date (UTC)	Exp. (ks)	State
VW Hyi	XMM-Newton	EPIC/PN	0111970301	2001-10-19 06:10:05	2001-10-19 10:38:34	14.5	quiescence
	Chandra*	LETG/HRC	21671	2018-08-08 00:16:30	2018-08-08 03:19:03	9.67	outburst
SS Cyg	XMM-Newton	EPIC/PN	0111310201	2001-06-05 08:14:19	2001-06-05 11:34:10	11.8	quiescence
	Chandra	LETG/HRC	1897	2001-01-16 21:13:00	2001-01-17 10:49:56	47.1	outburst
	Chandra	HETG/ACIS	646	2000-08-24 10:28:23	2000-08-25 00:19:30	47.3	quiescence
	Chandra	HETG/ACIS	648	2000-09-14 21:09:02	2000-09-15 14:15:05	59.5	outburst
	Chandra	HETG/ACIS	2307	2000-09-12 17:00:58	2000-09-13 03:47:18	36.6	outburst
	RXTE	PCA	50012-01-01-00	2000-08-24 13:04:16	2000-08-24 18:31:44	13.4	quiescence
	RXTE	HEXTE	50012-01-01-00	2000-08-24 13:04:16	2000-08-24 18:31:44	1.19	quiescence
	RXTE	PCA	10040-01-01-000	1996-10-09 16:47:28	1996-10-09 23:00:00	6.10	outburst
	RXTE	PCA	10040-01-01-001	1996-10-09 23:28:32	1996-10-10 07:25:36	11.4	outburst
	RXTE	PCA	10040-01-01-00	1996-10-10 07:25:20	1996-10-10 11:17:04	8.67	outburst
U Gem	XMM-Newton	EPIC/PN	0110070401	2002-04-13 05:35:37	2002-04-13 11:35:35	15.1	quiescence
	Chandra	LETG/HRC	3773	2002-12-25 19:50:15	2002-12-26 09:28:39	47.0	outburst
	Chandra	HETG/ACIS	647	2000-11-29 12:01:20	2000-11-30 15:13:31	94.9	quiescence
	Chandra	HETG/ACIS	3767	2002-12-26 09:28:39	2002-12-27 03:33:37	61.4	outburst
	RXTE	PCA/HEXTE	80011-01-02-00	2004-03-05 02:14:56	2004-03-05 09:03:44	14.5	outburst
SS Aur	XMM-Newton	EPIC/PN	0502640201	2008-04-07 08:40:28	2008-04-07 20:31:58	31.5	quiescence
	RXTE	PCA/HEXTE	30026-03-01-00	1998-01-24 05:03:12	1998-01-24 12:12:00	14.2	quiescence

* Observation not considered in our final analysis.

Standard filters were applied during data screening through the `evselect` task. We considered only single and doubles events (using `pattern ≤ 4`). `FLAG==0` was used to discard regions of the detector (like border pixels and columns with higher offset) for which the pattern type and the total energy is known with significantly lower precision.

The observation of SS Cyg is taken in Timing mode and prior 23rd of May 2012, period in which almost all EPIC-pn exposures are unexpectedly affected by X-ray loading (XRL) which occurs when source counts contaminates the offset map taken prior the exposure. Because of this we applied the XRL correction to this observation.

In all spectral extraction, the background region was selected from a region away from the source. The distribution matrix (`rmf`) and the ancillary (`arf`) files were created through the `rmfgen` and `arfgen` tasks. The final spectra were rebinned in order to have at least 25 counts for each background-subtracted channel.

CHANDRA

We used all 8 grating *Chandra* public observations of our nmCV sample presented to the preparation time of this paper, see Table 1 for a log of the observations. VW Hyi was observed only once during an outburst, while SS Cyg and U Gem were observed four and three times, respectively, in both outburst and quiescence states. SS Aur does not have public observations available in the archive. SS Cyg, U Gem and VW Hyi were observed once in LETG/HRC-S mode, while SS Cyg and U Gem were

observed 3 and 2 times in HETG/ACIS-S mode, respectively. Following the standard procedure³, we used CIAO v4.11 and the corresponding calibration files to reprocess the data. The spectra of each observation were generated with the *Chandra_repro* script. We combined the first order spectra together and adopted a minimum signal-to-noise value of 10 to group the spectra. We also extracted for each observation two light curves in 0.4-4 keV and 4-10 keV bands, and checked for variability. Significant changes in the HR were not observed and therefore we used the total exposure time in the spectral extraction. The reprocessed spectrum of VW Hyi did not show a spectral component at energies greater than 0.5 keV. Therefore, we did not consider this spectrum in our final spectral analysis.

RXTE

We have analyzed 6 *RXTE* observations of three nmCVs: one of U Gem, one of SS Aur, and four of SS Cyg. SS Aur and SS Cyg Obs. ID 50012-01-01 were observed in quiescence. All other observations were taken with the source in outburst state. See Table 1 for a log of the observations.

All PCA data was analyzed following the standard procedure. Only low resolution (16 s) light curves were produced together with spectra in the 2–60 keV band. For each observation, spectra and light curves were derived using standard *RXTE*/FTOOLS. Briefly, the data reduction consists of the source + background production, with subsequent subtraction of the PCA background estimated through the PCABACKEST tool. The PCA response matrix was built with PCARSP, and a systematic errors (off 0.04%) were added to each individual spectrum.

HEXTE 20–200 keV spectrum extraction (Rothschild et al. 1998) is done using comparison, for each cluster, the spectra from two separate background fields that are sampled alternately during observations. This capability allowed us, for example, in discarding data from cluster B for SS Cyg, since one of the background regions for this cluster (and for that sky position) is contaminated by the nearby source IGR J21485+4306. HEXTE background lines (Rothschild et al. 1998) were also treated and removed from the final spectrum. Spectra and response matrices were produced following the well-known procedures (see, e.g., D’Amico et al. 2001).

4. SPECTRAL ANALYSIS

In order to validate the Comptonization framework in nmCVs and to obtain better estimates of the physical parameters and spectral (photon) indices in these systems, we analyzed spectra of our sources obtained by three different observatories – *XMM-Newton*, *Chandra* and *RXTE*. All analyses were performed using XSPEC astrophysical package version 12.8.2.

The spectral continuum was first modeled by a single thermal Comptonization component, COMPTT model in XSPEC (Titarchuk 1994; Hua & Titarchuk 1995; Titarchuk & Lyubarskij 1995), considering a plasma cloud of a plane geometry. The physical free parameters of this model are: the temperature of the seed photons, kT_s , the electron temperature kT_e and the optical depth τ of the Compton cloud. Only when required by the fit, a second Comptonization component was added to the total model. Due to the broader spectral energy range of *RXTE*, this second component was required only in three out of four *RXTE* spectra of SS Cyg.

In all *XMM-Newton*, *Chandra* and *RXTE* spectra, the residual excess – i.e., the emission lines – expected and observed in the Fe XXI–XXVI K-shell (~ 6.4 – 7.0 keV) energy range was modeled by

³ <https://cxc.harvard.edu/ciao/threads/gspec.html>

up to three Gaussian components. Due to the low energy resolution of *RXTE/PCA*, only one broad Gaussian component is required to account for the excess caused by these features.

XMM-NEWTON SPECTRAL ANALYSIS

In all spectra, an addition of a photo-electric absorption (N_H) and/or a blackbody component (e.g., BBODY or BBODYRAD model) did not improve the fit performed in the $\sim 0.3 - 15/0.4 - 10$ keV energy range of *XMM-Newton*.

The spectrum of U Gem showed three iron emission lines, with centroid energies of: $6.394^{+0.013}_{-0.013}$ keV (at 2.5 sigma of the He-like K_α line), $6.68^{+0.04}_{-0.04}$ keV (compatible with He-like Fe K_α line) and $6.972^{+0.023}_{-0.019}$ keV (at 1.2 σ from the H-like Fe K_α line at 7.0 keV); and equivalent widths (EWs) of 53^{+41}_{-25} eV, 281^{+100}_{-49} eV and 167^{+53}_{-40} eV, respectively.

The spectra of SS Cyg and SS Aur showed two iron emission lines. In SS Cyg, the lines appear with centroid energies of $6.634^{+0.026}_{-0.023}$ keV (compatible with neutral Fe K_α line) and $6.966^{+0.030}_{-0.026}$ keV (at 1.1 σ from the H-like Fe K_α line at 7.0 keV); and EWs of 186^{+321}_{-27} eV and 75^{+97}_{-20} eV, respectively.

In SS Aur, the lines appear with centroid energies of $6.67^{+0.04}_{-0.03}$ keV (compatible with He-like Fe K_α line) and $7.00^{+0.05}_{-0.05}$ keV (compatible with H-like Fe K_α line); with EWs of 528^{+388}_{-156} eV and 169^{+99}_{-89} eV, respectively.

The VW Hyi spectrum is the only one that showed one emission iron line. This line appears with a Gaussian centroid energy of $6.672^{+0.017}_{-0.015}$ keV (at 1.6 σ from the He-like Fe K_α line); and it is very strong, with EW equal to 995^{+152}_{-143} eV, which is 2–20 times stronger than those observed in other sources.

Table 2 shows the best-fit parameters and fit quality found for each *XMM-Newton* observation, and Figure 2 shows the best spectral fits. The presence of the Fe Gaussian lines are evident in all fits. Without adding any model to account for the iron line emission, the best-fit gives a reduced $\chi^2_{\text{red}} = \chi^2/\text{degree of freedom (d.o.f)}$ of 1.54 (801/521) for VW Hyi, 1.38 (1151/836) for SS Cyg, 1.97 (530/269) for U Gem and 1.11 (672/604) for SS Aur. When Gaussian components were added to the fit, it leads to a χ^2_{red} of 1.30 (672/519) for VW Hyi, 1.01 (840/831) for SS Cyg, 1.15 (366/317) for U Gem and 0.93 (556/598) for SS Aur.

In addition to the emission iron lines in the $\sim 6.4 - 7.0$ keV energy range, we observed in all spectra another strong and broad residual excess peaked at ~ 1.01 keV, with Gaussian centroid in the $\sim 0.96 - 1.02$ keV energy range (see the Gaussian₀ component in Table 2). These centroid energies are compatible with resonance lines emitted by Ne X, Fe XVII or Fe XXI ions. Table 3 summarizes these possible emission lines.

We determined the range of physical parameters given by the COMPTT model:

- The temperature kT_s of the seed photons ranges from 0.056 to 0.174 keV.
- The electron temperature, kT_e of the Comptonization cloud ranges from 5.99 to 8.72 keV.
- The optical depth τ of the Comptonization cloud ranges from 2.65 to 4.73.

CHANDRA SPECTRAL ANALYSIS

The residual broad excess around 1 keV observed in all *XMM-Newton* spectra was also observed in three out of five HETG/ACIS *Chandra* spectra analysed in this paper. This feature and the

Table 2. Spectral analysis of the *XMM-Newton* observations of our nmCVs sample. Our model to fit the spectra: COMPTT+GAUSSIAN₀+GAUSSIAN₁+GAUSSIAN₂+GAUSSIAN₃.

Source			VW Hyi	SS Cyg	U Gem	SS Aur
Component	Parameter	Unit				
CompTT	kT_s	keV	$0.15^{+0.01}_{-0.01}$	$0.100^{+0.021}_{-0.044}$	$0.141^{+0.004}_{-0.004}$	$0.168^{+0.006}_{-0.007}$
	kT_e	keV	$8.58^{+0.14}_{-0.14}$	$7.64^{+0.05}_{-0.05}$	$6.43^{+0.06}_{-0.06}$	$6.12^{+0.13}_{-0.13}$
	τ		$2.72^{+0.07}_{-0.07}$	$4.49^{+0.05}_{-0.05}$	$4.65^{+0.08}_{-0.08}$	$4.56^{+0.15}_{-0.14}$
Gaussian ₀	E_L	keV	$1.017^{+0.013}_{-0.013}$	$0.971^{+0.013}_{-0.013}$	$1.004^{+0.017}_{-0.017}$	$0.987^{+0.024}_{-0.027}$
	σ	keV	$0.096^{+0.013}_{-0.013}$	$0.113^{+0.013}_{-0.012}$	$0.136^{+0.016}_{-0.014}$	$0.118^{+0.029}_{-0.027}$
	EW	eV	150^{+20}_{-19}	49^{+91}_{-15}	103^{+20}_{-20}	105^{+25}_{-24}
Gaussian ₁	E_L	keV			$6.394^{+0.013}_{-0.013}$	
	σ	keV			1.3×10^{-2a}	
	EW	eV			53^{+41}_{-25}	
Gaussian ₂	E_L	keV	$6.672^{+0.017}_{-0.015}$	$6.634^{+0.026}_{-0.023}$	$6.68^{+0.04}_{-0.04}$	$6.67^{+0.04}_{-0.03}$
	σ	keV	$1.27^{+0.02}_{-0.02} \times 10^{-2}$	$0.12^{+0.05}_{-0.05}$	1.3×10^{-2a}	$8^{+6}_{-6} \times 10^{-2}$
	EW	eV	995^{+152}_{-143}	186^{+322}_{-27}	281^{+100}_{-49}	528^{+388}_{-156}
Gaussian ₃	E_L	keV		$6.966^{+0.030}_{-0.026}$	$6.972^{+0.023}_{-0.019}$	$7.00^{+0.05}_{-0.05}$
	σ	keV		5×10^{-2b}	2.3×10^{-2a}	1.5×10^{-3a}
	EW	eV		75^{+97}_{-20}	167^{+53}_{-40}	169^{+99}_{-89}
Fit quality	$\chi^2/\text{d.o.f}$		672/519	840/831	366/317	556/598
	χ^2_{red}		1.30	1.01	1.15	0.93
Energy range		keV	0.3 – 15.0	0.7 – 10.0	0.3 – 15.0	0.3 – 15

Uncertainties at 90% confidence level.

a Parameter pegged at hard limit.

b Parameter frozen.

narrow emission lines (narrow excesses $\gtrsim 2\sigma$) present in the Chandra spectra were modeled by simple Gaussian components. U Gem has one HETG/ACIS observation in quiescence and one in outburst state, whereas SS Cyg was observed once in quiescence and twice in outburst state.

Fitting the continuum with only one COMPTT component without adding any component to account for the emission lines, the best-fit gives a χ^2_{red} of 1.85 (131/71) and 2.57 (321/125) for U Gem Obs. ID 647 and 3767, respectively; and 1.24 (589/478), 2.5 (421/168), and 1.57 (143/91) for SS Cyg Obs. ID 646, 648, and 2307, respectively. When Gaussian components were added to the fit, it leads to a χ^2_{red} of 1.03 (67/65) and 1.01 (114/113) for U Gem Obs. ID 647 and 3767, respectively; and 0.97 (453/467), 0.80 (121/151), and 0.64 (52/81) for SS Cyg Obs. ID 646, 648, and 2307, respectively.

Table 3. Emission lines compatible with the line centroid energy of the Gaussian component fit to the broad residual excess (in the 0.8 to 1.2 keV energy range) present in the soft X-ray spectra of all nmcVs analyzed.

Ion	Transition	Energy (keV)	$\lambda(A^\circ)$	DNe
Ne X	1s - 2p	1.022	12.131	VW Hyi, U Gem
Fe XVII	$2p^6 \ ^1S - 2p^5 4s^1 P$	0.976	12.703	SS Cyg, SS Aur
	$2p^6 \ ^1S - 2p^5 4d^1 P$	1.023	12.119	VW Hyi
Fe XXI	$2s^2 2p^2 \ ^3P - 2s 2p^2 3p^3 P$	0.992	12.498	SS Aur, U Gem
	$2p^2 \ ^3P - 2p 3d^3 D$	1.008	12.300	VW Hyi, U Gem, SS Aur

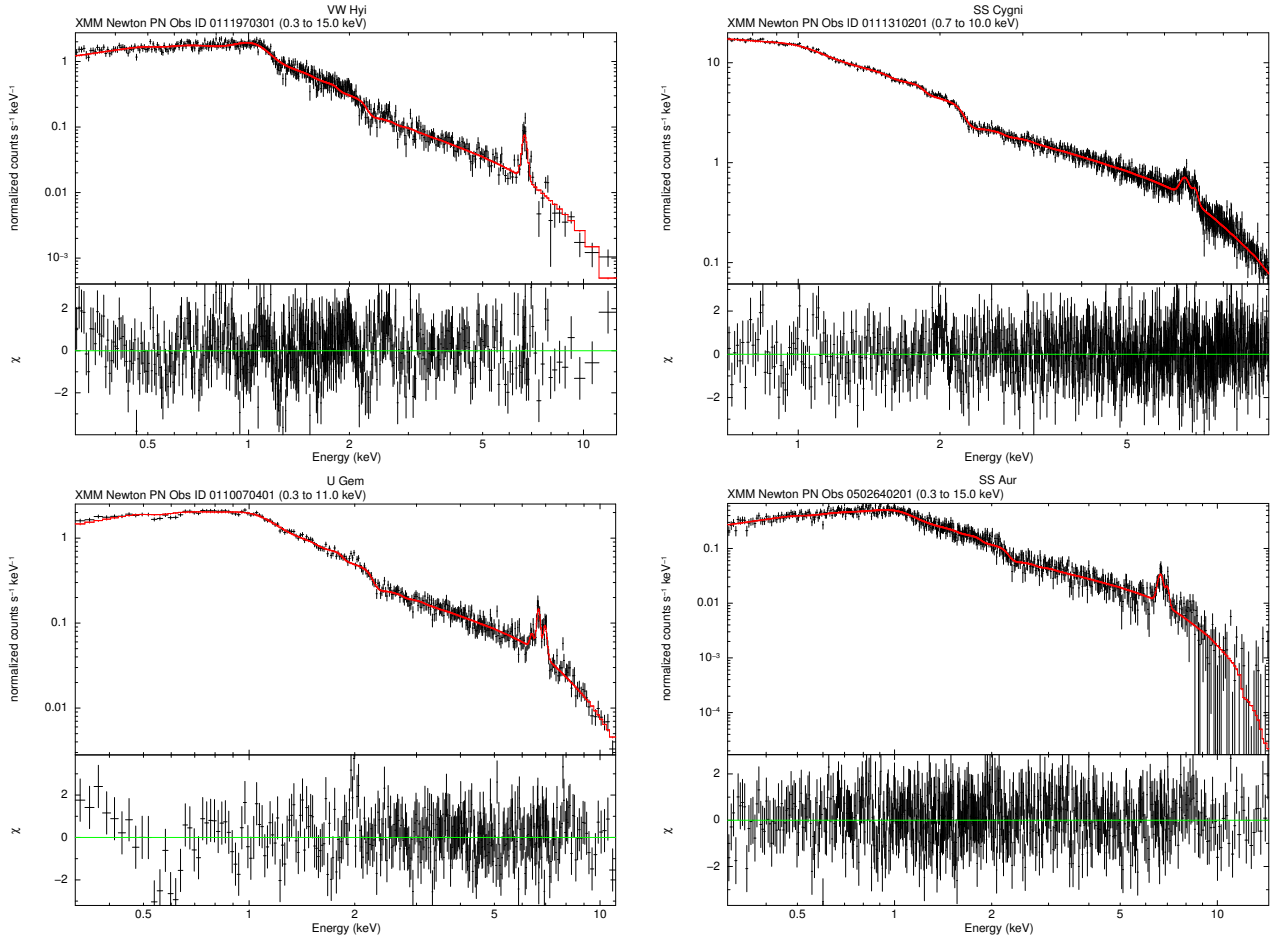


Figure 2. XMM Newton EPIC pn spectra of the four non-magnetic CVs analyzed. *Left top panel:* spectrum of VW Hyi in the 0.3-15.0 keV energy range, the data (*in black*) and the total model COMPTT+GAUSSIAN+GAUSSIAN (*solid red line*). *Left lower panel:* spectrum of U Gem in the 0.3-15.0 keV energy range, the data (*in black*) and the best fit model COMPTT+GAUSSIAN+GAUSSIAN+GAUSSIAN+GAUSSIAN (*solid red line*). *Right top panel:* spectrum of SS Cyg in the 0.7-10.0 keV energy range, the data (*in black*) and the best fit model COMPTT+GAUSSIAN+GAUSSIAN+GAUSSIAN (*solid red line*). *Right lower panel:* spectrum of SS Aur in the 0.3-15 keV energy range, the data (*in black*) and the best fit model COMPTT+GAUSSIAN+GAUSSIAN+GAUSSIAN (*solid red line*). The lower panels show the residuals of the data vs. model

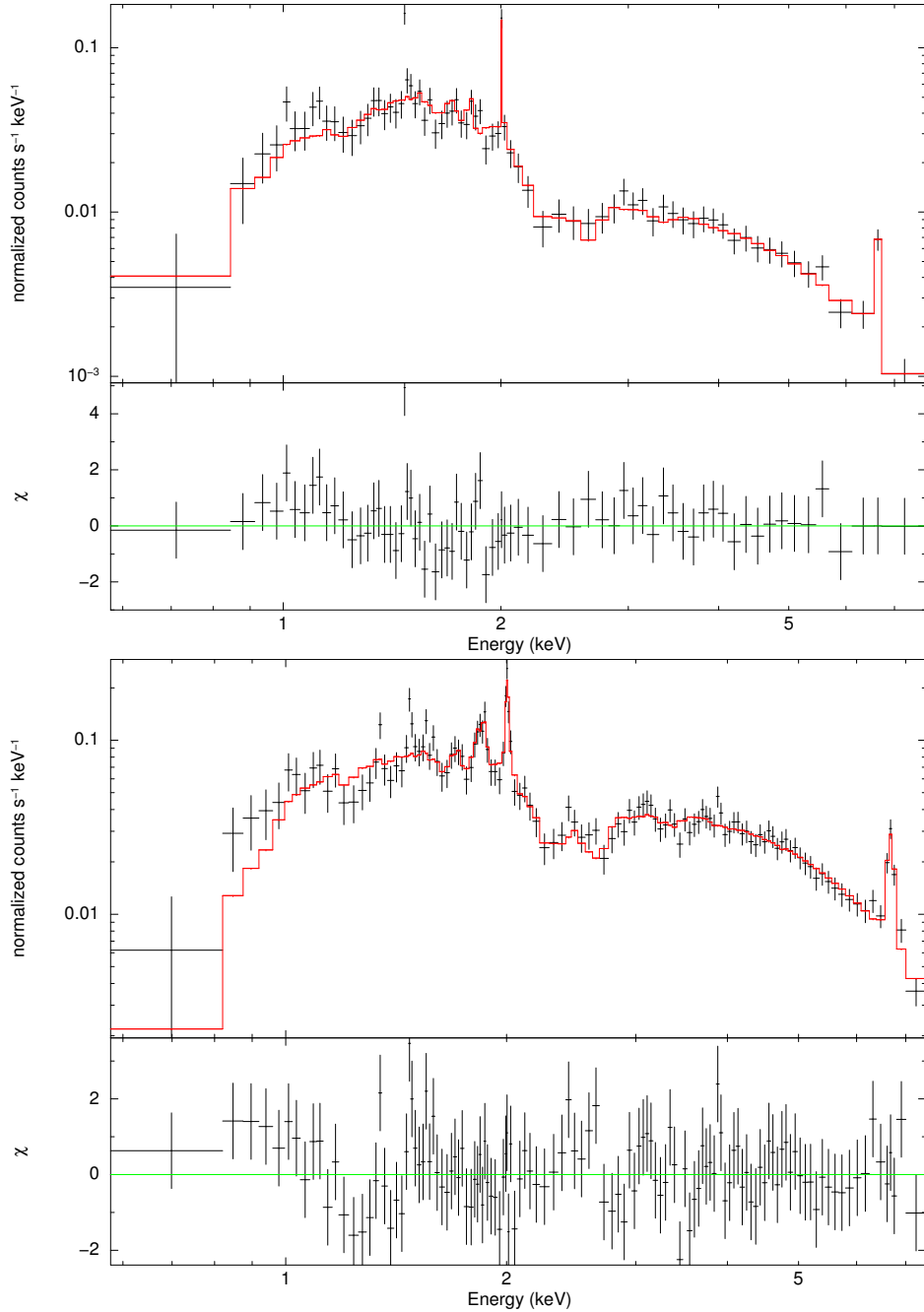


Figure 3. Chandra HETG/ACIS spectra of U Gem in the 0.4-10 keV energy range. *Upper panel:* spectral fit to Obs. ID 647 (see Table 4, column 4), the data (*in black*) and the total model COMPTT+GAUSSIAN+GAUSSIAN (*solid red line*). *Bottom panel:* spectral fit to Obs. ID 3767 (see Table 4, column 5), the data (*in black*) and the best fit model COMPTT+GAUSSIAN+GAUSSIAN+GAUSSIAN+GAUSSIAN components (*solid red line*). The lower panels show the residuals of the data vs. model.

Table 4 and 5 show the best-fit parameters and fit quality for each spectrum of U Gem and SS Cyg, respectively. Figures 3–4 show spectral fits.

In U Gem, the values of the temperature kT_e and τ parameters, agree at 90% confidence level, in the two observations: τ is ~ 5 , and kT_e is equal to $5.0^{+0.5}_{-0.5}$ keV and 6^{+5}_{-2} keV in Obs. 647 (in

Table 4. Spectral analysis of the *Chandra* HETG/ACIS observations of U Gem, using pure thermal COMPTT and Gaussian components.

Component	Parameter	Unit	Obs. ID 647	Obs. ID 3767
CompTT	kT_s	keV	$0.087_{-0.010}^{+0.004}$	$0.66_{-0.10}^{+0.12}$
	kT_e	keV	$5.0_{-0.5}^{+0.5}$	6_{-2}^{+5}
	τ		$5.1_{-0.3}^{+0.3}$	5_{-1}^{+1}
Gaussian ₀	E_L	keV	$6.63_{-0.07}^{+0.08}$	$6.68_{-0.02}^{+0.02}$
	σ	keV	$0.06_{-a}^{+0.04}$	$0.06_{-0.02}^{+0.02}$
Gaussian ₁	E_L	keV	$2.006_{-0.001}^{+0.004}$	$2.004_{-0.005}^{+0.001}$
	σ	keV	$2_{-a}^{+1} \times 10^{-3}$	$9_{-3}^{+3} \times 10^{-3}$
Gaussian ₂	E_L	keV		$1.86_{-0.01}^{+0.01}$
	σ	keV		$1.5_{-0.4}^{+0.5} \times 10^{-2}$
Gaussian ₃	E_L	keV		1.00^b
	σ	keV		$0.24_{-0.06}^{+0.07}$
Fit quality	$\chi^2/\text{d.o.f}$		67/65	114/113
	χ_{red}^2		1.03	1.01
Energy range		keV	0.4 – 10	0.4 – 10

Uncertainties at 90% confidence level.

a Parameter pegged at hard limit.

b Parameter frozen.

quiescence) and 3767 (in outburst), respectively. On the other hand, a value of the temperature kT_s of the seed photons in Obs. 3767 ($0.66_{-0.10}^{+0.12}$ keV) appears ~ 8 times greater than the temperature in Obs. 647 ($0.66_{-0.10}^{+0.12}$ keV). For the two observations, the total model led to χ_{red}^2 of 1.0 (see Table 4).

In SS Cyg, independently of the source state, the best-fits were found in general by a COMPTT component with kT_s of 0.10 keV, kT_e of ~ 5 keV, and τ of ~ 6 . It is important to stress that initially all parameters were considered as a free one, however, the electron temperature kT_e appears not well constrained by the fits – it either assumed values greater than the upper limit given by the *Chandra* effective energy band (8 keV), or lower than the minimum value acceptable by the Comptonization model (5 keV, see Hua & Titarchuk (1995)). Therefore, this parameter was kept fixed in the three fits. The spectrum of Obs. 648 is the only one which shows a very low seed photon temperature kT_s of $0.020_{-0.003}^{+0.004}$ keV – the presence of many lines in the soft energy band of this spectrum may affect the value of this parameter. We obtained a χ_{red}^2 of ~ 1.0 for the fit to Obs. 646, and lower than 1.0 for Obs. 648 and 2307 (see Table 5).

The LETG/HRC spectra of SS Cyg and U Gem were not successfully described by only one thermal Comptonization component. Moreover, a presence of many lines in the 0.07-2 keV energy band makes a problem to satisfactory fit the data. For example, a good fit in terms of χ^2 -statistic ($\chi_{red}^2 < 2$) is

obtained when the soft energy band ($E < 2.5$ keV in SS Cyg and $E < 1.5$ keV in U Gem, respectively) is not taken into account. In this case, fitting SS Cyg and U Gem spectra with a thermal COMPTB component (Farinelli et al. 2008) and two Gaussian components – with centroid energies at 1.86 and 2.005 keV – led to χ^2_{red} of 1.34 (16/12) and 1.33 (47.9/36), correspondingly.

EMISSION LINES IN THE HETG/ACIS SPECTRA

The broad residual excess peaked around ~ 1 keV, observed in all *XMM-Newton* Epic-pn spectra, was also observed in the *Chandra* spectra of U Gem Obs. ID 3767 in outburst, and SS Cyg Obs. ID 648 and 2307 (in outburst). This broad excess could be an emission from Fe XVII, Fe XXI, or Ne X ions (see Table 3). However, the fit of this feature with a Gaussian component led to lower centroid energies. In U Gem Obs. ID 3767, the Gaussian line energy is frozen at 1.0 keV, with σ equal to $0.24^{+0.07}_{-0.06}$ keV (see Table 4). In SS Cyg Obs. ID 648 and 2307, it is equal to $0.87^{+0.03}_{-0.04}$ keV and $0.93^{+0.04}_{-0.05}$ keV, respectively; with σ equal to $0.15^{+0.03}_{-0.02}$ keV and $0.10^{+0.04}_{-0.03}$ keV, respectively (see Table 5). Table 6 summarizes the possible resonance narrow emission lines observed in the *Chandra* HETG/ACIS spectra. In U Gem (see Table 4), the spectrum of Obs. ID 647 shows two emission lines, with centroid energies at $6.63^{+0.08}_{-0.07}$ keV (compatible with He-like K_α Fe line at 6.7 keV) and $2.006^{+0.004}_{-0.001}$ keV (compatible with Si XIV, at 2.007 keV). The spectrum Obs. ID 3767 shows three emission lines, with centroid energies at $6.68^{+0.02}_{-0.02}$ keV (compatible with He-like K_α Fe line), $2.004^{+0.001}_{-0.005}$ keV (at 3σ of Si XIV line), and $1.86^{+0.01}_{-0.01}$ keV (compatible with Si XIII, at 1.865 keV).

In SS Cyg (see Table 5), the spectrum of Obs. 646 shows only the three iron lines in the 6.4-7.0 keV energy range: at $6.39^{+0.01}_{-0.01}$ keV (compatible with neutral K_α Fe line), $6.67^{+0.01}_{-0.02}$ keV (at 3σ of the He-like K_α Fe line), and $6.97^{+0.01}_{-0.03}$ (at 3σ of the H-like K_α Fe line). The spectrum of Obs. 648 shows in total six emission lines, with centroid energies at: $0.87^{+0.03}_{-0.04}$ keV (compatible with emission from either Ca XVIII, Fe XVII, Ni XIX, or Ni XVIII; see Table 6), $1.346^{+0.004}_{-0.004}$ keV (compatible with emission from Mg XI at 1.343, and 1.5σ from the 1.352 keV line), $1.473^{+0.004}_{-0.005}$ (compatible with emission from Mg XII, at 1.473), $1.859^{+0.003}_{-0.004}$ keV (at 2 sigma of Si XIII emission), $2.005^{+0.003}_{-0.004}$ keV (compatible with Si XIV emission), and $6.65^{+0.03}_{-0.04}$ keV (at 1.7σ from the He-like K_α Fe line). The spectrum of Obs. 2307 shows in total four emission lines, with centroid energies at: $0.93^{+0.04}_{-0.05}$ keV (compatible with Ca XVIII, Ni XIX, and Ne IX), $1.472^{+0.008}_{-0.007}$ keV (compatible with Mg XII), $1.857^{+0.005}_{-0.005}$ keV (at 1.6σ from the Si XIII line), and $6.61^{+0.01}_{-0.01}$ keV (at 1.7σ from the Fe XXII K_α line at 6.627 keV), see Table 6.

RXTE SPECTRAL ANALYSIS

Almost all observations showed a low count rate (< 1 cts/s) in the energy band > 25 keV of the PCA spectra. The same, or no counts, were observed in the 40-150 keV of the HEXTE spectra. Therefore, except for Obs. ID 50012-01-01-00 of SS Cyg, we performed the spectral analysis considering only the PCA spectra with energy range up to 25 keV.

Because *RXTE* Obs. ID 50012-01-01-00 of SS Cyg is simultaneous to *Chandra* Obs. ID 646, we have analysed the 0.4-8 keV HETG/ACIS *Chandra* spectral band together with the 8-60 keV PCA and 60-150 keV HEXTE energy band of *RXTE*.

The spectrum of U Gem Obs. ID 80011-01-02-00, SS Aur Obs. ID 30026-03-01-00, and SS Cyg Obs. ID 10040-01-01-000 were well described, in the ~ 5 –25 keV energy band, by only one COMPTT component. On the other hand, the other three spectra of SS Cyg (Obs. ID 50012-01-01-00, 10040-01-01-001, and 10040-01-01-00) required a second spectral component. For all these three observations,

Table 5. Spectral analysis of the *Chandra* HETG/ACIS observation of SS Cyg, using thermal COMPTT and Gaussian components.

Component	Parameter	Unit	Obs. ID 646	Obs. ID 648	Obs. ID 2307
CompTT	kT_s	keV	$0.10^{+0.05}_{-a}$	$0.020^{+0.004}_{-0.003}$	$0.11^{+0.01}_{-0.01}$
	kT_e	keV	5.0^b	5.0^b	5.0^b
	τ		$5.9^{+0.1}_{-0.1}$	$7.2^{+0.3}_{-0.3}$	$5.7^{+0.3}_{-0.3}$
Gaussian ₀	E_L	keV		$0.87^{+0.03}_{-0.04}$	$0.93^{+0.04}_{-0.05}$
	σ	keV		$0.15^{+0.03}_{-0.02}$	$0.10^{+0.04}_{-0.03}$
Gaussian ₁	E_L	keV		$1.346^{+0.004}_{-0.004}$	
	σ	keV		$1.09^{+0.6}_{-0.3} \times 10^{-2a}$	
Gaussian ₂	E_L	keV		$1.473^{+0.004}_{-0.005}$	$1.472^{+0.008}_{-0.007}$
	σ	keV		$1.2^{+0.4}_{-0.3} \times 10^{-2a}$	$1.0^{+0.8}_{-0.6} \times 10^{-2}$
Gaussian ₃	E_L	keV		$1.859^{+0.003}_{-0.004}$	$1.857^{+0.005}_{-0.005}$
	σ	keV		$1.3^{+0.3}_{-0.2} \times 10^{-2}$	$1.4^{+0.4}_{-0.3} \times 10^{-2}$
Gaussian ₄	E_L	keV		$2.005^{+0.003}_{-0.004}$	
	σ	keV		$1.3^{+0.3}_{-0.3} \times 10^{-2a}$	
Gaussian ₅	E_L	keV	$6.39^{+0.01}_{-0.01}$	$6.65^{+0.03}_{-0.04}$	$6.61^{+0.01}_{-0.01}$
	σ	keV	0.02^b	$0.08^{+0.08}_{-0.09}$	0.02^b
Gaussian ₆	E_L	keV	$6.67^{+0.01}_{-0.02}$		
	σ	keV	0.03^b		
Gaussian ₇	E_L	keV	$6.97^{+0.01}_{-0.03}$		
	σ	keV	0.02^b		
Fit quality	$\chi^2/\text{d.o.f}$		453/467	121/151	52/81
	χ^2_{red}		0.97	0.80	0.64
Energy range		keV	0.4 – 8.0	0.4 – 10	0.4 – 10

Uncertainties at 90% confidence level.

a Parameter pegged at hard limit.

b Parameter frozen.

we fit a model consisting of (1) a blackbody (BBODY) plus a Comptonization (COMPTT) component or (2) a sum of two Comptonization (COMPTT) components.

In general, taking into account the χ^2 -statistic and the range of physical parameters, the best fits were found for the second case – that is, when two COMPTT components were used to describe the total spectra. Namely, the best-fits were found when both the electron temperature kT_e and the

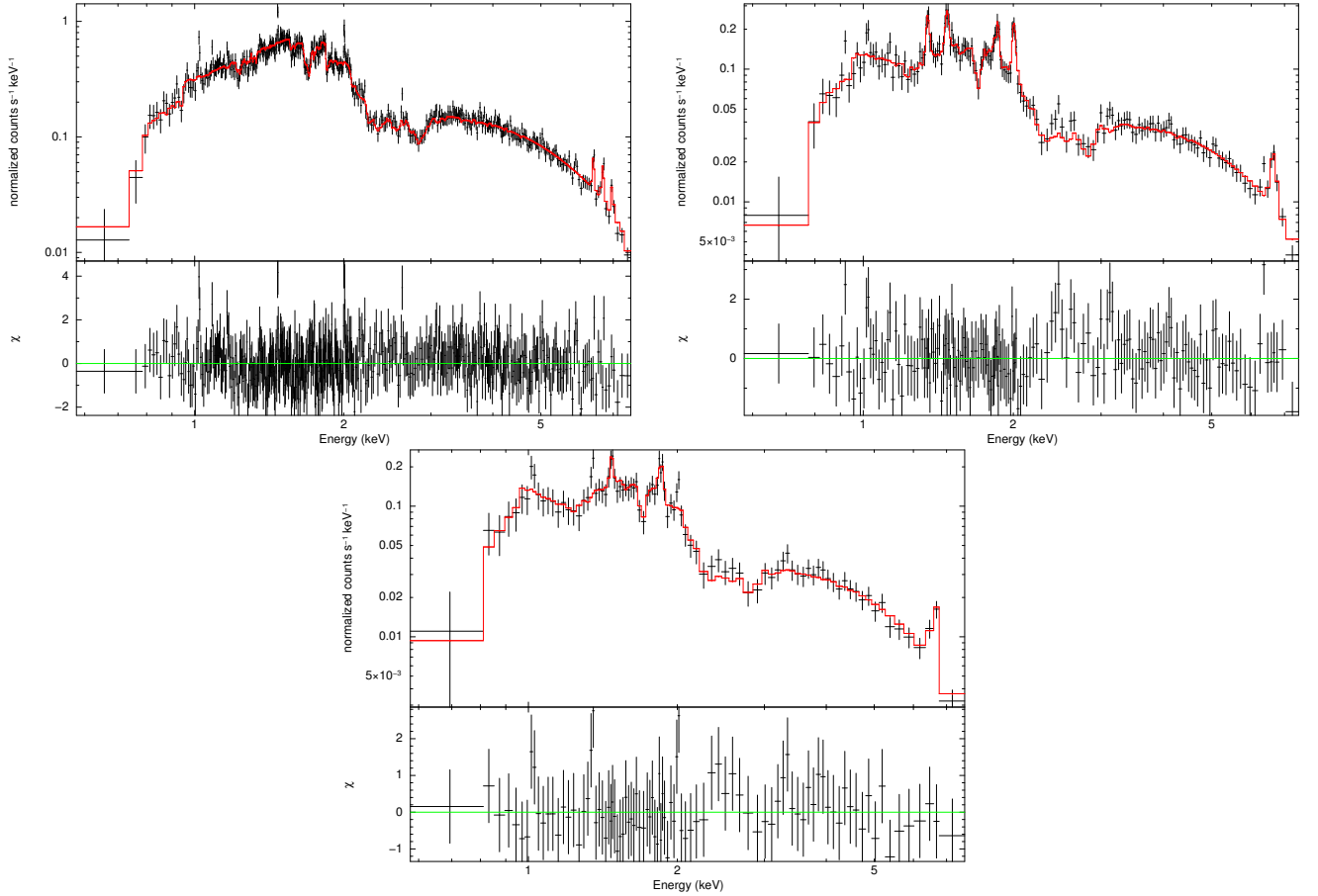


Figure 4. Chandra HETG/ACIS spectra of SS Cyg in the 0.4-10 keV energy range. *Left top panel:* spectral fit to Obs. ID 646 (see Table 5, column 4), the data (*in black*) and the total model COMPTT+GAUSSIAN+GAUSSIAN+GAUSSIAN (*solid red line*). *Right top panel:* spectral fit to Obs. ID 648 (see Table 5, column 5), the data (*in black*) and the best fit model COMPTT+GAUSSIAN+GAUSSIAN+GAUSSIAN+GAUSSIAN+GAUSSIAN+GAUSSIAN (*solid red line*). *Lower panel:* spectral fit to Obs. ID 2307 (see Table 5, column 6), the data (*in black*) and the total model COMPTT+GAUSSIAN+GAUSSIAN+GAUSSIAN+GAUSSIAN (*solid red line*). The lower panels in these plots show the residuals of the data vs. model.

optical depth τ of the COMPTT model were tied between the two components. Figure 5 shows the the geometry of our Comptonization model. We definitely establish that there is a disk which supplies the seed photons for the transition layer (Compton cloud). While red lines indicate the trajectories of the photons which illuminate the transition layer coming from the white dwarf (WD) surface. As a result the emergent X-ray spectrum formed in the transition layer as a result of up-scattering of the seed photons of the disk and WD surface off hot electrons of the Compton cloud.

In order to assess the statistical significance of the second COMPTT component, we computed the probability of chance improvement of the χ^2 by means of an F-test. It is worth stressing that the F-test to be used in this case is not the one that uses the $\Delta\chi^2$ as test statistics (let us call it *independent* F-test, or I-F-test for short). Indeed, in order to correctly use the I-F-test, the χ^2 variables must be linearly independent. In our case the two components share some parameters, therefore are not independent by construction, and therefore we must use another test statistics: the *dependent* F-test

Table 6. X-ray lines, other than the iron lines expected in the 6.4–7.0 keV energy range, compatible with the centroid energy of a Gaussian component present in the *Chandra* HETG/ACIS spectra.

Ion	Transition	Energy (keV)	$\lambda(A^\circ)$	DNe	Obs.ID
Ca XVIII	$2s - 4p$	0.886	13.993	SS Cyg	648, 2307
Fe XVII	$2s^6 - 2p^5 3d^1 P$	0.826	15.010	SS Cyg	648
Ni XIX	$2p^6 - 2p^5 3s^3 P$	0.884	14.025	SS Cyg	648, 2307
Ni XVIII	$2s^6 - 3s^2 S - 2p^5 3s^2 {}^2P$	0.879	14.105	SS Cyg	648
Ne IX	$1s^2 {}^1S - 1s 2p^1 P$	0.921	13.461	SS Cyg	2307
Mg XI	$1s^2 {}^1S - 1s 2p^3 P$	1.343	9.232	SS Cyg	648
Mg XI	$1s^2 {}^1S - 1s 2p^1 P$	1.352	9.170	SS Cyg	648
Mg XII	$1s - 2p$	1.473	8.417	SS Cyg	648, 2307
Si XIII	$1s^2 {}^1S - 1s 2p^1 P$	1.865	6.648	U Gem	3767
				SS Cyg	648, 2307
Si XIV	$1s - 2p$	2.007	6.177	U Gem	647, 3767
				SS Cyg	648
Fe XXII	K_α	6.627	1.871	SS Cyg	2307

(D-F-test for short). This test statistics is defined in terms of the ratio between the normalized χ^2 (see, eg, Barlow 1989; Press et al. 1992), and has been already successfully used for the assessment of the statistical significance of multiplicative components (that, too, are dependent components by construction) by Orlandini et al. (2012) and Iyer et al. (2015) among others.

The probability of chance improvement of the χ^2 by adding the second COMPTT component, evaluated by means of a D-F-test, is equal to 3×10^{-8} in SS Cyg Obs 50012-01-01-00, 0.07 in Obs. 10040-01-01-001, and 0.02 in Obs. 10040-01-01-00.

From these values we see that the second COMPTT component is statistically significant (equivalent to 5.4σ for a one-tailed test) only for the 50012-01-01-00 SS Cyg observation. This does not mean that this component is not present also in the other two *RXTE* observations, but only that the SNR in those two latter observations does not allow its detection above a confidence level of about 2σ .

Table 7 shows the best-fit parameters and fit quality for each source and observation. Figure 6 shows the spectral fits to U Gem and SS Aur. Figure 7 shows the spectral fits to the three observations of SS Cyg in outburst. It is important to stress that these three observations are consecutive. Figure 8 shows the spectral fit to the 0.4–150 keV simultaneous *Chandra/RXTE* spectra of SS Cyg in quiescence. Finally, Figure 9 shows the photon index Γ as a function of the best-fit electron temperatures kT_e of the TL for all sources analyzed using our nmCV sample.

Because of the low energy resolution of PCA, the emission iron lines expected in the ~ 6.4 – 7.0 keV energy range are not well resolved. Therefore, only one Gaussian component is required to account for the excesses in this energy range. Table 8 shows the line energy found for each observation, wherein for the simultaneous *Chandra/RXTE* spectra we exceptionally show the three iron emission lines observed by HETG/ACIS *Chandra*.

5. THE TRANSITION LAYER IN A WD AND SPECTRAL INDEX OF THE EXPECTED EMERGENT SPECTRUM IN THE COMPTONIZATION SCENARIO

Table 7. Spectral analysis of *RXTE* observations using thermal COMP_{TT} component(s).

Obs. ID	U Gem	SS Aur	SS Cyg	SS Cyg	SS Cyg	SS Cyg	SS Cyg	
State	80011-01-02-00	30026-03-01-00	50012-01-01-00	10040-01-01-000	10040-01-01-001	10040-01-01-001	10040-01-01-00	
Component	Parameter	Unit	Parameter	Unit	Parameter	Unit	Parameter	Unit
CompTT ₁	KT _{s1}	keV	0.23 ^{+0.03} _{-0.03}	0.05 ^{+0.01} _{-0.01}	0.11 ^{+0.06} _{-0.06}	0.20 ^{+0.01} _{-0.01}	0.31 ^{+0.05} _{-0.05}	0.29 ^{+0.03} _{-0.03}
	KT _{e1}	keV	43 ⁺⁵ ₋₄	37 ⁺⁶ ₋₅	32.8 ^{+0.5} _{-0.6}	25 ⁺¹ ₋₁	5.3 ^{+0.3} _{-0.3}	5.4 ^{+0.3} _{-0.3}
CompTT ₂	τ_1		0.83 ^{+0.26} _{-0.16}	1.0 ^{+0.1} _{-0.1}	1.21 ^{+0.01} _{-0.01}	1.82 ^{+0.06} _{-0.06}	4.8 ^{+0.2} _{-0.2}	4.5 ^{+0.2} _{-0.2}
	norm ₁		4 ⁺¹ ₋₁ × 10 ⁻⁴	8 ⁺¹ ₋₁ × 10 ⁻⁴	3.65 ^{+0.04} _{-0.04} × 10 ⁻³	1.02 ^{+0.03} _{-0.03} × 10 ⁻³	4 ⁺¹⁸ ₋₁ × 10 ⁻³	8.1 ^{+0.7} _{-0.7} × 10 ⁻³
CompTT ₂	KT _{s2}	keV		0.89 ^{+0.02} _{-0.02}			0.65 ^{+0.03} _{-0.03}	0.76 ^{+0.04} _{-0.04}
	KT _{e2}	keV		= KT _{e1}			= KT _{e1}	= KT _{e1}
Fit quality	τ_2			= τ_1			= τ_1	= τ_1
	norm ₂			5.0 ^{+0.1} _{-0.1} × 10 ⁻⁴			3 ⁺³ ₋₂ × 10 ⁻³	2 ⁺³ ₋₁ × 10 ⁻³
Energy range	$\chi^2/\text{d.o.f}$		38/36	40/53	503/554	42/46	42/44	50/44
	χ^2_{red}		1.06	0.88	0.91	0.91	0.94	1.13
			5 – 25	2.5 – 25	0.4 – 150	2.5 – 25	2.5 – 25	2.5 – 25

Uncertainties at 90% confidence level. The respective emission lines present in the spectra are presented in Table 8.

^a Parameter pegged at hard limit.

* Simultaneous *RXTE*/*Chandra* observation.

Table 8. Spectral analysis of the *RXTE* observations: Gaussian component(s).

Obs. ID	U Gem	SS Aur	SS Cyg	SS Cyg	SS Cyg	SS Cyg
80011-01-02-00	30026-03-01-00	50012-01-01-00	10040-01-01-000	10040-01-01-000	10040-01-01-001	10040-01-01-00
State	outburst	quiescence	quiescence*	outburst	outburst	outburst
Component	Parameter	Unit				
Gaussian ₁	E_{L1}	keV	$6.54^{+0.05}_{-0.06}$	$6.39^{+0.01}_{-0.01}$	$6.68^{+0.09}_{-0.09}$	$6.64^{+0.03}_{-0.03}$
	σ_{L1}	keV	$0.36^{+0.05}_{-0.06}$	$1.8^{+1.1}_{-1.7} \times 10^{-2}$	$0.38^{+0.12}_{-0.12}$	$0.33^{+0.05}_{-0.05}$
Gaussian ₂	E_{L2}	keV	$6.63^{+0.14}_{-0.13}$	$6.67^{+0.01}_{-0.02}$		$6.64^{+0.03}_{-0.03}$
	σ_{L2}	keV	$0.32^{+0.19}_{-a} \times 10^{-2}$	$3.4^{+1.6}_{-1.1} \times 10^{-2}$		$0.33^{+0.04}_{-0.04}$
Gaussian ₃	E_{L3}	keV		$6.97^{+0.01}_{-0.02}$		
	σ_{L3}	keV		$2.12^{+0.02}_{-a} \times 10^{-2}$		

Uncertainties at 90% confidence level.

a Parameter pegged at hard limit.

* Simultaneous Chandra/RXTE (Obs. ID 646/50012-01-01-00) spectra. The lines present in the HETG/ACIS *Chandra* spectrum are shown.

Table 9. Best-fitting plasma temperature kT in the nmCVs of our sample obtained by thermal Comptonization (this paper) and some previous modeling (see section 2).

Source	State	kT^* (keV)	Spectral Model	Observatory	Reference	
U Gem	q [†]	20	MKCFLOW	Chandra/HETG	Mukai et al. (2003) (Obs. ID 647)	
	q	55^{+10}_{-10}	MKCFLOW	XMM-Newton/EPIC	Pandel et al. (2005)	
	q	15 – 38	CEMEKL, MKCFLOW	XMM-Newton/EPIC, Chandra/HETG	Güver et al. (2006) (Obs. ID 0110070401, 647)	
	o [‡]	5.4 – 29	CEMEKL	Chandra/HETG	Güver et al. (2006) (Obs. ID 3767)	
	q	$25.82^{+1.98}_{-1.43}$	MKCFLOW	XMM-Newton/EPIC	Byckling et al. (2010)	
	q	$0.78^{+0.03}_{-0.01}$	MEKAL	XMM-Newton/EPIC	Byckling et al. (2010)	
	q	$16.5^{+4.49}_{-3.31}$	APEC	SUZAKU/XIS	Xu et al. (2016)	
	q	$6.43^{+0.06}_{-0.06}$	COMP TT	XMM-Newton/EPIC	this paper (Obs. ID 0110070401)	
	q	$5.0^{+0.5}_{-0.5}$	COMP TT	Chandra/HETG	this paper (Obs. ID 647)	
	o	6^{+5}_{-2}	COMP TT	Chandra/HETG	this paper (Obs. ID 3767)	
o	43^{+5}_{-4}	COMP TT	RXTE/PCA	this paper (Obs. ID 80011-01-02-00)		
SS Cyg	q	80	MKCFLOW	Chandra/HETG	Mukai et al. (2003) (Obs. ID 646)	
	q	$20.4^{+4.0(stat)+3.0(sys)}_{-2.6(stat)+3.0(sys)}$	CVMEKAL	SUZAKU/XIS	Ishida et al. (2009)	
	o	$6.0^{+1.3}_{-0.2}$	CVMEKAL	SUZAKU/XIS	Ishida et al. (2009)	
	q	$10.44^{+0.16}_{-0.17}$	MEKAL	SUXAKU/XIS	Byckling et al. (2010)	
	q	$41.99^{+1.20}_{-0.76}$	MKCFLOW	SUXAKU/XIS	Byckling et al. (2010)	
	o	$8.15^{+1.23}_{-0.91}$	APEC	SUZAKU/XIS	Xu et al. (2016)	
	q	$7.64^{+0.05}_{-0.05}$	COMP TT	XMM-Newton/EPIC	this paper (Obs. ID 0111310201)	
	q	5**	COMP TT	Chandra/HETG	this paper (Obs. ID 646)	
	o	5**	COMP TT	Chandra/HETG	this paper (Obs. ID 648)	
	o	5**	COMP TT	Chandra/HETG	this paper (Obs. ID 2307)	
o	25^{+1}_{-1}	COMP TT	RXTE/PCA	this paper (Obs. ID 10040-01-01-000)		
o	$5.3^{+0.3}_{-0.3}$	COMP TT	RXTE/PCA	this paper (Obs. ID 10040-01-01-001)		
o	$5.4^{+0.3}_{-0.3}$	COMP TT	RXTE/PCA	this paper (Obs. ID 10040-01-01-00)		
q	$32.8^{+0.5}_{-0.6}$	COMP TT	Chandra/RXTE [§]	this paper [§]		
VW Hyi	q	> 5	Bremsstrahlung	EXOSAT	van der Woerd & Heise (1987)	
	q	$2.17^{+0.15}_{-0.15}$	Raymond-Smith	ROSAT	Belloni et al. (1991)	
	?	4 – 10	two- MEKAL or Raymond-Smith	ASCA	Hasenkopf & Eracleous (2002)	
	q	6 – 8	CEMEKL, CEVMKL and MKCFLOW	XMM-Newton/EPIC	Pandel et al. (2003) (Obs. ID 0111970301)	
	q	$8.2^{+0.3}_{-0.3}$	MKCFLOW	XMM-Newton/EPIC	Pandel et al. (2005) (Obs. ID 0111970301)	
	q	$5.79^{+4.71}_{-2.14}$	APEC	SUZAKU/XIS	Xu et al. (2016)	
	q	$8.58^{+0.14}_{-0.14}$	COMP TT	XMM-Newton/EPIC	this paper (Obs. ID 0111970301)	
	q	5-9	CEVMKL, VMCFLOW	XMM-Newton/EPIC SUZAKU/XIS	Nakaniwa et al. (2019) (Obs. ID 0111970301)	
	SS Aur	q	$6.35^{+0.40}_{-0.40}$	MEKAL	SUZAKU/XIS	Byckling et al. (2010)
		q	$23.47^{+4.01}_{-3.02}$	MKCFLOW	SUZAKU/XIS	Byckling et al. (2010)
q		$8.48^{+5.34}_{-2.61}$	APEC	SUXAKU/XIS	Xu et al. (2016)	
q		$6.12^{+0.13}_{-0.13}$	COMP TT	XMM-Newton/EPIC	this paper (Obs. ID 0502640201)	
q		37^{+6}_{-5}	COMP TT	RXTE/PCA	this paper (Obs. ID 30026-03-01-00)	

* For multi-temperature plasma models, the temperature kT correspond to the maximal temperature (kT_{\max}) to that the plasma is heated up.

** Parameter frozen.

† Source observed in quiescence state.

‡ Source observed in outburst state.

§ Simultaneous Chandra HETG/ACIS Obs. ID 646 and *RXTE* (PCA and HEXTE) Obs. ID 50012-01-01-00.

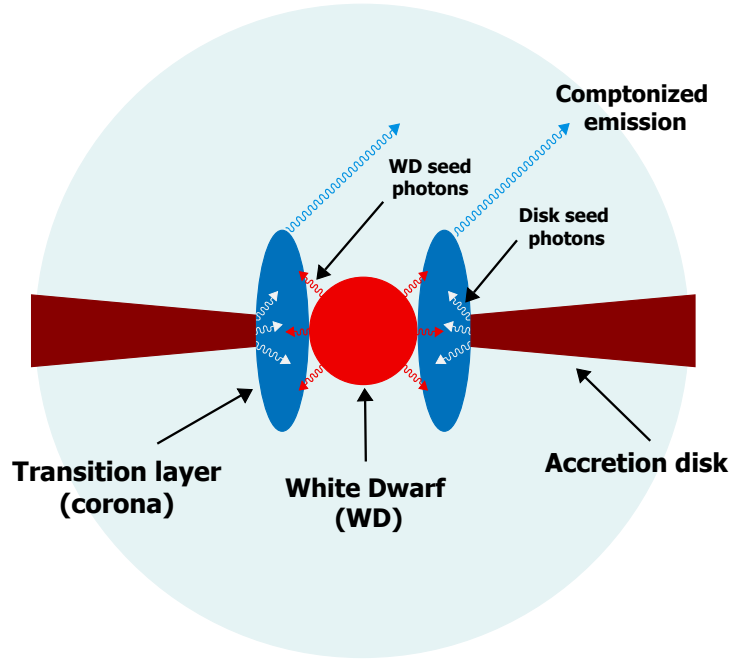


Figure 5. Geometry of the Comptonization framework in nMCVs. Both the seed photons coming from the inner part of the accretion disk and the seed photons coming from (or close) the white dwarf surface are up-scattered by thermal electrons present in the transition layer (or corona), which is located between the WD surface and the accretion disk. The light blue sphere around the system represents the region wherein relatively cold material is outflowing, where lines are formed.

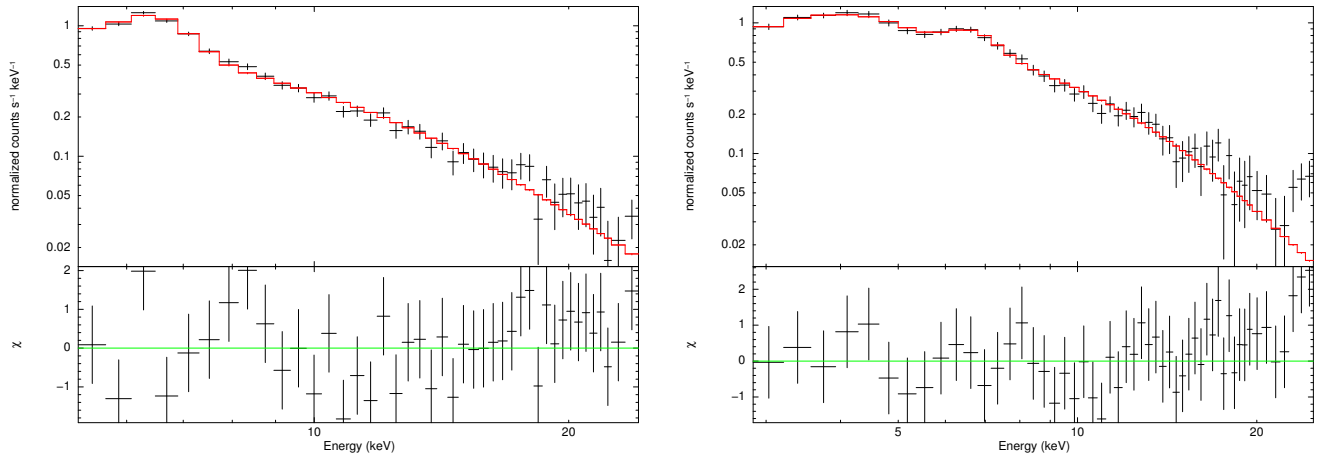


Figure 6. Spectral fits of the *RXTE*/PCA data for U Gem in outburst (*left panel*) and SS Aur in quiescence (*right panel*). The solid *red* line shows the total COMPTT+GAUSSIAN model (see Table 7 and 8). The lower panels show the residuals of the data vs. model.

As Farinelli & Titarchuk (2011), hereafter FT11, pointed out the energy release in the TL of a NS determines the spectral index of the emergent spectrum. In similar way we use the TL model to estimate the index for a case of a WD. But in this case instead of the reflection inner boundary of the TL at a NS we use the pure absorption boundary at a WD. FT11 demonstrated that the energy

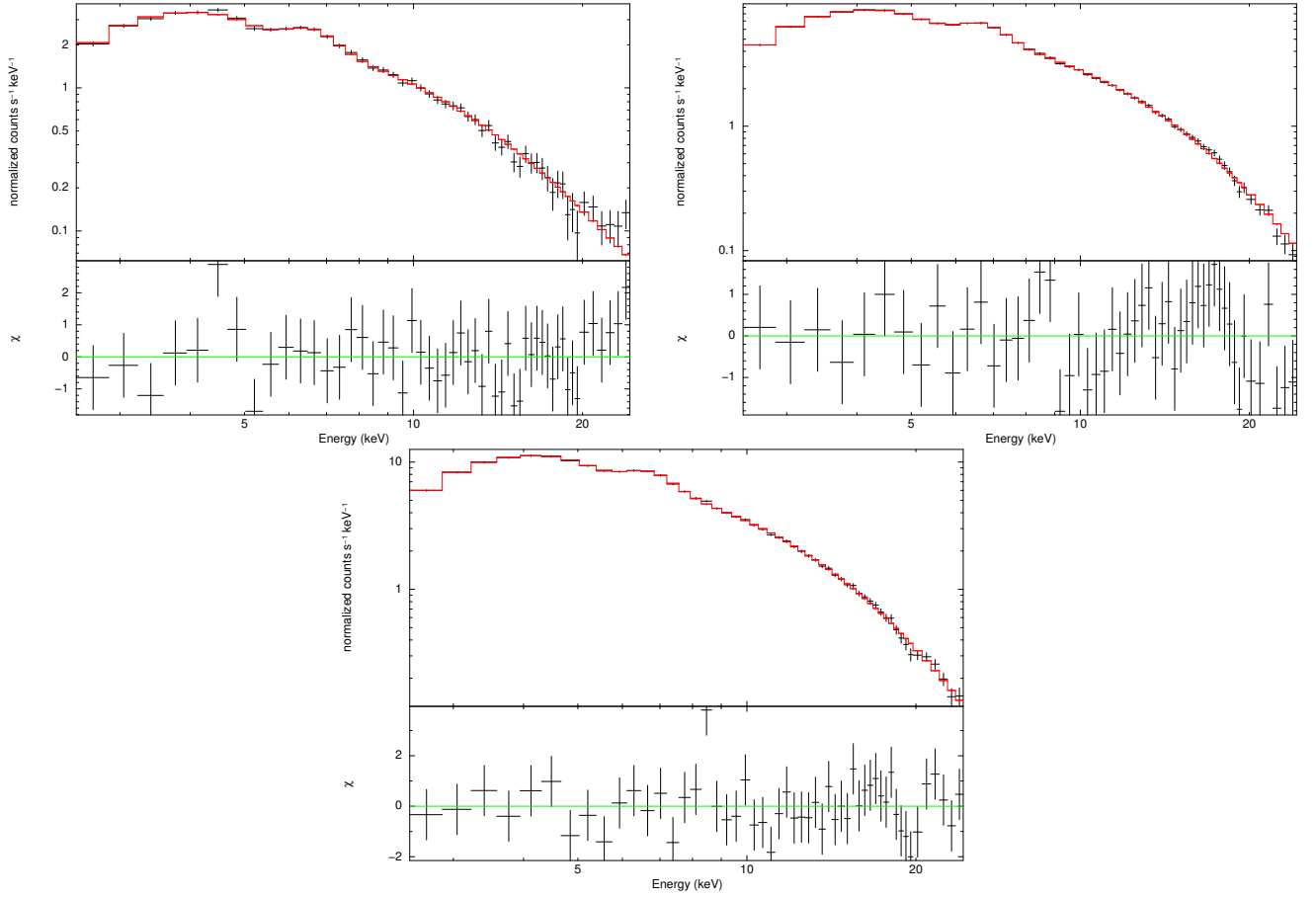


Figure 7. Spectral fits to the *RXTE*/PCA spectra of SS Cyg in outburst: Obs. ID 10040-01-01-000 (*left top panel*), 10040-01-01-001 (*right top panel*), and (10040-01-01-00 *lower panel*). The solid red line shows the COMP TT+GAUSSIAN total model in Obs. ID 10040-01-01-000, and COMP TT+COMP TT+GAUSSIAN in Obs. ID 10040-01-01-001 and 10040-01-01-00 (see Table 7 and 8). The lower panels show the residuals of the data vs. model.

flux per unit surface area of the TL (corona) can be found as

$$Q_{cor} = 20.2 \int_0^{\tau_0} \varepsilon(\tau) T_e(\tau) d\tau, \quad (1)$$

where $T_e(\tau)$, $\varepsilon(\tau)$ and τ_0 are the plasma (electron) temperature, the radiation density distributions in the TL and its Thomson optical depth, respectively.

We obtain the energy distribution $\varepsilon(\tau)$ as a solution of the diffusion equation

$$\frac{d^2\varepsilon}{d\tau^2} = -\frac{3Q_{cor}}{c\tau_0} \quad (2)$$

where c is the speed of light.

We should also add the two boundary conditions at the inner TL boundary, which can be an absorbed surface at WD $\tau = \tau_0$ and the outer boundary $\tau = 0$. They are correspondingly:

$$\frac{d\varepsilon}{d\tau} + \frac{3}{2}\varepsilon|_{\tau=\tau_0} = 0, \quad (3)$$

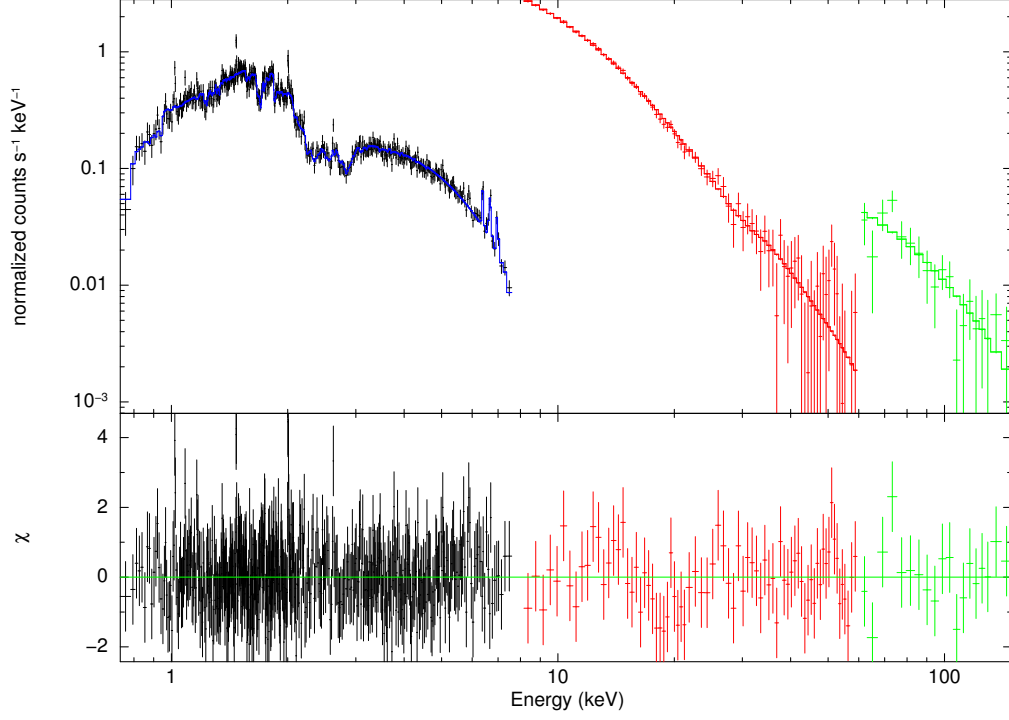


Figure 8. Spectral fit to the simultaneous *Chandra/RXTE* (Obs. ID 646/Obs. ID 50012-01-01-00) spectra of SS Cyg, using the `COMPTT+COMPTT+GAUSSIAN+GAUSSIAN+GAUSSIAN` total model. The *black*, *red* and *green* points correspond to 0.4-8.0 keV HETG/ACIS, 8.0-60 keV PCA and 60-150 keV HEXTE data, respectively. The *blue*, *red* and *green* lines correspond to the best spectral fit (see column 6 of Table 7 and 8). The lower panel show the residuals of the data vs. model

$$\frac{d\varepsilon}{d\tau} - \frac{3}{2}\varepsilon|_{\tau=0} = 0. \quad (4)$$

We find the solution $\varepsilon(\tau)$ of equations (2-4)

$$\varepsilon(\tau) = \frac{Q_{cor}}{c} \{1 + 3/2 \tau_0 [(\tau/\tau_0) - (\tau/\tau_0)^2]\} \quad (5)$$

Thus integration of $\varepsilon(\tau)$ gives us

$$\int_0^{\tau_0} \varepsilon(\tau) d\tau = \frac{Q_{cor}}{c} \tau_0 (1 + \tau_0/4). \quad (6)$$

Now we can estimate the Comptonization Y-parameter in the TL using Eqs. (1) and (6). We rewrite Eq. (1) using the mean value theorem as

$$Q_{cor} = 20.2 \hat{T}_e \int_0^{\tau_0} \varepsilon(\tau) d\tau \quad (7)$$

where \hat{T}_e is the mean electron temperature in the TL.

Substitution of formula (6) in Eq. (7) leads to the following estimate (Y-parameter) in the TL [see a definition of Y-parameter in Rybicki & Lightman (1979)]

$$\frac{k \hat{T}_e \tau_0 (\tau_0/4 + 1)}{m_e c^2} = 0.25 \quad (8)$$

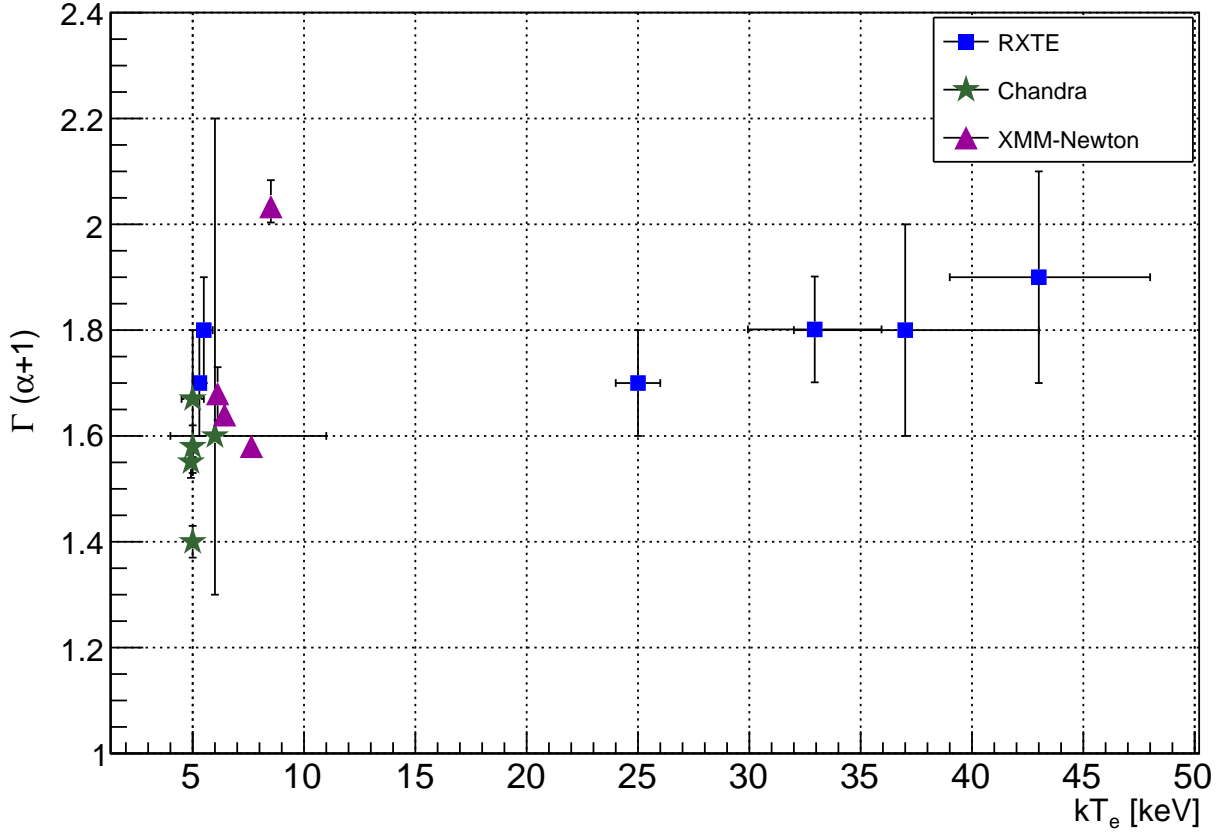


Figure 9. Photon indices Γ vs. the best-fit electron temperatures kT_e in the Compton cloud (Transition layer): the blue, green and magenta points correspond to *RXTE*, *Chandra* and *XMM-Newton* spectra analyzed, respectively (see Tables 2, 4, 5 and 7).

As we can see in Figure 9, the photon index, Γ shows only small deviations from 1.8: namely, for most of our sources $\Gamma = 1.8 \pm 0.1$, while the Compton cloud electron temperature varies from 5 to 45 keV. In some sense this index behavior is similar to that observed in NSs (Titarchuk et al. 2014).

As already pointed out in classical work (Farinelli & Titarchuk 2011), spectral formation in plasma clouds of finite size (bounded medium) is related to the distribution law of the number of scatterings that seed photons experience before their escape. If u_{av} denotes the average number of photon scatterings and the dimensionless scattering number is $u = N_e \sigma_T c t$, then the distribution law for $u \gg u_{av}$ is given by (Sunyaev & Titarchuk 1980, 1985)

$$P(u) = A(u, \tau_0) e^{-\beta u}. \quad (9)$$

For a diffusion regime when $\tau_0 > 1$, the corresponding $\beta = \lambda_1^2/3$, where λ_1 is the first eigenvalue of the diffusion space operator. As reported in Sunyaev & Titarchuk (1985), the eigenvalue problem for photon diffusion in a slab with the total optical depth, τ_0 is derived from a solution of the differential equation for the zero-moment intensity

$$\frac{d^2 J}{d\tau^2} + \lambda^2 J = 0, \quad (10)$$

with boundary conditions $dJ/d\tau - (3/2)J = 0$ and $dJ/d\tau + (3/2)J = 0$, for $\tau = 0$ and $\tau = \tau_0$, respectively. This leads to the transcendental equation for the eigenvalue λ_n , $n = 1, 2, 3, \dots$

$$\tan(\lambda_n \tau_0 / 2) = \frac{2}{3\lambda_n}, \quad (11)$$

which has the solution for $n = 1$

$$\lambda_1 = \frac{\pi}{2(\tau_0/2 + 2/3)}. \quad (12)$$

But the spectral index α (photon index $\Gamma = \alpha + 1$) is

$$\alpha = -3/2 + (9/4 + \beta/\theta)^{1/2} \quad (13)$$

where $\beta = \lambda_1^2/3$ and $\theta = kT_e/(m_e c^2)$ (Sunyaev & Titarchuk 1980). Thus

$$\alpha = -3/2 + (9/4 + \pi^2/[12(\tau_0/2 + 2/3)^2\theta])^{1/2} \quad (14)$$

and using Equation (8) we obtain that $\alpha \lesssim 0.85$ (or $\Gamma \lesssim 1.85$). This is precisely what we observed (see Fig. 9).

6. DISCUSSION

As previously mentioned, the Comptonization model is not the standard radiative one currently used for the description of the continuum in nmCVs. On the other hand, the Comptonization model is the standard one for fitting the LMXBs spectra.

Considering that nmCVs share similarities with LMXBs – that is, they have an accretion disk, a compact object and a TL (corona) (which presence is evident from observation of non-eclipsed UV emission lines in eclipsing systems (see, e.g., Warner 1995; Mauche & Raymond 2000)) – we look for spectral similarities between these two types of X-ray binaries. That is, our main goal is to seek a common physical process able to describe the continuum of both nmCVs and LMXBs.

Figure 5 represents the Comptonization framework in nmCVs, in which the emission lines are produced far from the most central part of the system where the X-ray continuum is produced.

Because of the broad spectral X-ray energy band of PCA and HEXTE instruments, we have also analyzed some of *RXTE* observations of our source sample which is available in the archive (see Table 1), including a simultaneous 0.4–150 keV *Chandra/RXTE* spectra of SS Cyg in quiescence state. The broadband, including harder (> 15 keV) X-rays, can provide a better understanding of this scenario and physical parameters in terms of the Comptonization framework in these sources – mainly the electron temperatures and spectral indices.

All sources in our sample were observed in the quiescence state by *XMM-Newton* Epic-pn. We found that only one thermal Comptonization component plus Gaussian components successfully fit the *XMM-Newton* Epic pn spectra of two nmCVs: SS Cyg and SS Aur. In terms of χ^2 -statistics, our model did not provide a perfect description of the VW Hyi and U Gem *XMM-Newton* total spectra. In these two cases, the value of χ^2 exceeds the critical value at 0.01 level of significance. However,

the spectral analyses of U Gem using *Chandra* and *RXTE* data show a satisfactory fit (see Table 4 and 7 column 4). It is likely that the presence of several emission lines, besides the iron complex, in the *XMM-Newton* spectra of VW Hyi and U Gem worsened the fit quality.

It is important to emphasize that all *XMM-Newton* spectral fits show best-fit parameters with a mean seed photon temperature $\langle kT_s \rangle$ of 0.14 ± 0.01 keV, a mean optical depth $\langle \tau \rangle$ of 4.1 ± 0.5 , and a mean electron temperature $\langle kT_e \rangle$ of 7.2 ± 0.6 keV. The spectral fits performed in the 1.5 to 15 keV energy range of the *XMM-Newton* spectra does not allow accurately estimate the temperature of the seed photons. In this case, the parameters appeared with a mean value $\langle kT_s \rangle$ of 0.25 ± 0.05 keV, $\langle \tau \rangle$ of 4.5 ± 0.5 , and $\langle kT_e \rangle$ of 5.9 ± 0.5 keV. Therefore, we obtained a better description of the seed photon temperature when considering the total Epic pn spectral band in our analyses.

The *Chandra* HETG/ACIS spectra show parameters similar to those found by *XMM-Newton*, with a mean $\langle kT_s \rangle$ of 0.20 ± 0.12 keV, a mean optical depth $\langle \tau \rangle$ of 5.2 ± 0.2 , and a mean electron temperature $\langle kT_e \rangle$ of 5.8 ± 0.4 keV. SS Cyg was observed once in the quiescence state and twice in the outburst state by *Chandra*. We did not obtain a perfect fit for the two observations in outburst (see Table 5). In addition, we did not observe a difference on the spectral continuum parameters between the two states. This can be due to the *Chandra* effective energy band (< 8 keV). Namely, we found that the electron temperature in the *Chandra* spectra are not very well constrained by these fits.

In the analyses of the *RXTE* spectra, a second Comptonization component was necessary for the description of the total spectrum in three observation of SS Cyg. In these cases, a satisfactory spectral fit was found if, both kT_e and the optical depth τ of the COMPTT model were tied between the two components. Namely, it means that the total ~ 0.4 –150 keV or 2.5–25 keV spectra of all analysed nmCVs are characterized by only one spectral index α ($\alpha = \Gamma - 1$).

The *RXTE* spectra of our sample showed a wide range of the electron temperatures, kT_e laying in the 5–48 keV range. When one compares values of α (or Γ) between the different sources (see Table 7, Fig. 9), he/she does not find any correlation of kT_e with Γ . It is also worth noting that SS Cyg shows $kT_e \sim 5$ keV in outburst, U Gem shows kT_e of 43_{-4}^{+5} keV also in outburst state, and SS Aur shows a temperature of 37_{-5}^{+6} keV in the quiescence state. Therefore, we establish that we do not find any correlation of the kT_e with the spectral state using the data of our set of CVs. For sake of comparison, we present in Table 9 the best-fitting plasma temperature found by our analyses together with the ones reported by some previous spectral modeling, for all CVs in our sample (see section 2). As shown in Table 9, the spectral modeling present in the literature is not homogeneous and no clear correlation of the plasma temperature with spectral stage is found between the sources in previous spectral modeling as well.

In the *RXTE* spectra, the first Comptonization component shows a mean value of the seed photon temperature kT_{s1} of 0.20 ± 0.04 keV. This temperature appears higher in the observations in outburst. SS Cyg shows $kT_{s1} \sim 2$ –3 times higher when in outburst. It is important to point out, however, that the *RXTE* data do not precisely determine the seed photon temperatures if their values are much less than 1 keV because the lower limit of the *RXTE* data is ~ 3 keV. Therefore, all values of the seed photons kT_s obtained through *RXTE* data (see Table 7) are upper limits.

In the three *RXTE* observations of SS Cyg for which the second Comptonization component was required, the seed photon temperature kT_{s2} of the second component appears with a mean value of 0.77 ± 0.07 keV. This component is not observed at the very early stage of the optical outburst, but

reappears in the consecutive observations increasing its value to $0.76_{-0.04}^{+0.04}$ keV in the last observation, closer to the outburst optical peak. In the observation of the quiescence state, kT_{s2} is equal to $0.89_{-0.02}^{+0.02}$ keV. We, therefore, did not observe a huge difference in the temperature kT_{s2} between the different states. Interestingly, the *Chandra* spectrum of U Gem Obs. ID 3767 in outburst (see Table 4) shows a single Comptonization component with the seed photon temperature of $0.66_{-0.10}^{+0.12}$ keV. A transient hard component was reported in U Gem during its 2004 outburst (see section 2.1 and (Güver et al. 2006)) and associated with the outburst state. We, on the other hand, observed this hard component also during the quiescence state in SS Cyg. This is an evidence that this hard X-ray component is not a spectral feature of outburst states only.

In the Comptonization framework, the seed photons are up-scattered (Comptonized) by hot electrons of a Compton cloud around the compact object (ST80). Our analyses showed that there are up to two seed photon components in nmCVs presumably coming from the internal and outer parts of the TL. The corresponding components are the results of the Comptonization of these soft photons, characterized by their color temperature kT_{s1} and kT_{s2} , in the TL located between the WD surface and the inner part of the accretion disk. The electrons in the TL are characterized by a single electron temperature as clearly showed by our analyses of the *RXTE* spectra.

The source of hard X-rays in quiescence is compact, as observed by X-ray light curves of eclipsing DNe (see, e.g. Mukai 2017; Lewin & van der Klis 2006, and references therein). Therefore, the Comptonized cloud (TL) should be compact. In our interpretation, the seed photon component showing lowest temperatures ($kT_{s1} \sim 0.1\text{--}0.2$ keV) is coming from the inner part of the accretion disk, while the second and transient component related to kT_{s2} is coming from a more internal part of the system, closer or from the WD surface.

We tested, for the *XMM-Newton* and *RXTE* spectra, if an addition of an interstellar absorption component (TBABS model in XSPEC) would result in lower temperatures. We freeze the interstellar absorption parameter (NH) to the value expected in the line of sight of the source. In the *XMM-Newton* spectra, we easily obtained satisfactory fits for VW Hyi, U Gem and SS Aur sources. In these cases, kT_{s1} assumed values of ~ 0.01 keV, but in addition to the observed increase of χ^2_{red} , this parameter was not well constrained by the fit. In the *RXTE* spectra, the inclusion of the TBABS component did not change the best-fit parameters. We obtained the same result when setting NH as a free parameter: in some of the fits it assumed at a very low value of 10^{19} atoms cm^{-2} , and did not affect the best-fit parameters in all fits.

Figure 8 shows the total 0.4–150 keV spectrum of SS Cyg in quiescence. This spectrum corresponds to the simultaneous observations of *Chandra* HETG/ACIS Obs. ID 646 and *RXTE* (PCA and HEXTE) Obs. ID 50012-01-01-00. It is important to point out that the spectral analysis considering the simultaneous hard X-ray spectral band (> 15 keV) of *RXTE* is superior and of great importance to constrain the physical parameters – e.g., the temperature of the electrons in the TL ($kT_e = 33_{-3}^{+3}$ keV) and the spectral index ($\Gamma = 1.8_{-0.1}^{+0.1}$), since considering only the HETG/ACIS spectrum it leads to lower values of kT_e and Γ ($kT_e = 5$ keV and $\Gamma = 1.55_{-0.03}^{+0.02}$); whereas the soft spectral band of *Chandra* allows a better determination of the seed photons temperature kT_{s1} (see Table 5 and 7).

The possible change in the spectral description in CVs (from optically thin thermal plasma to up-scattering of soft photons due to inverse Compton in a thick Comptonization cloud) is analogous to adopting the Comptonization model to describe LMXB spectra in the $\sim 3\text{--}50$ keV energy range – before Comptonization being broadly accepted, bremsstrahlung was the model used to describe the

spectra of LMXBs (see, e.g., D’Amico et al. 2001). In a similar way, bremsstrahlung is the radiative process on the basis of the MEKAL and the cooling flow models which have been used to fit the spectral continuum of CVs. In LMXBs the use of the Comptonization model were then extended to broader (from ~ 0.3 keV to ~ 250 keV) X-ray energy band (see, e.g., Di Salvo et al. 2006; D’Aí et al. 2007; Montanari et al. 2009; Maiolino et al. 2013; Titarchuk et al. 2014).

As we demonstrated in Fig. 9 the observed photon indices, Γ is distributed around 1.8 using the data for at least 15 spectra of nmCVs. Moreover, in the previous section 5 we theoretically estimate the photon index of the emergent spectrum, Γ which is formed in the TL around a WD. In order to do it we apply the radiative transfer formalism to solve the boundary problem for the energy density distribution in the TL around a WD (see Eqs. 2–5) and estimate the gravitational energy release, Q in the TL in order to find a Comptonization parameter presented by formula (8). Moreover, solving the eigenvalue problem for an average intensity $J(\tau)$ (see Eq. 10) and using a formula for the spectral index α ($\Gamma = \alpha + 1$), Eq. (13) along with an estimate (8) we obtain that the photon index Γ in the TL of an accreting WD should be around 1.85. This is a first principle estimate of the photon index which is really confirmed by our analysis of the nmCVs observations (see Fig. 9).

6.1. Emission lines and continuum

The total observed spectrum consists of the continuum and line photons emission. In the standard framework, since the total spectrum shows many lines coming from different elements and ionisation degree, optically thin plasma with different temperatures, besides the one driving the continuum emission, are needed to describe all the spectral features. The different plasma temperature regions are located outside of the TL where the continuum is produced. As previously mentioned, spectral fittings using a single optically thin plasma are also used to describe the total spectrum. Though it can lead to a satisfactory fit, in terms of χ^2 statistics, it can also lead to plasma temperatures too high to explain the presence of all emission lines. For example, for U Gem a best-fit plasma temperature of about 16.5 keV (see section 2.1 and Xu et al. (2016)) is reported, at this temperature the plasma would be completely ionized and no line(s) in the ~ 6.4 -6.7 keV range would be present. That is, at this temperature the ~ 6.4 -6.7 keV iron emission complex should not be produced in the same region of the X-ray continuum. Namely, much higher plasma temperatures are reported in IPs (Xu et al. 2016).

In the framework of the continuum production through the thermal Comptonization, the continuum is formed in the TL – in an optically thick medium, in both the quiescence and outburst states. The emission lines are likely produced in an optically thin region, located in an external region, far from the TL and the WD surface. In other words, the continuum is formed closer to the WD than the lines.

Optically thin thermal plasma and cooling flow codes make simultaneously fits of the continuum and the emission lines from several elements using a range of temperatures (or few components of optically thin thermal plasma of different temperatures). They satisfactory fit all (or almost all) excesses (features) superposing the continuum. For example, the MEKAL model includes ~ 2409 lines from all the 15 most important chemical elements (H, He, C, N, O, Ne, Na, Mg, Al, Si, S, Ar, Ca, Fe and Ni) and broad residual excesses might be fitted by several narrower emission lines. Changing a description of the continuum to the Comptonization one has a consequence that the residual excesses present in the spectra (i.e., the emission lines and their shape) will be directly observed after fitting

the continuum – as it is observed in LMXBs. In this case each of emission line should be independently identified and modeled using e.g., Gaussian components.

Applying a thermal Comptonization component (either COMPTT or COMPTB) to fit the continuum of the nMCVs, we have identified a broad and strong emission line peaked at $\sim 0.96\text{--}1.02$ keV in all *XMM-Newton* spectra. We fitted this residual excess present in the ~ 0.8 to 1.2 keV energy range with a single Gaussian line. We identified the centroid energy of the lines as being compatible with resonance lines emitted by Fe XXI (in SS Aur, U Gem and VW Hyi), and/or Fe XVII (in VW Hyi, SS Aur and SS Cyg), and/or Ne X line (in VW Hyi and U Gem) (see Table 3). This residual excess was also observed in one *Chandra* HETG/ACIS spectrum of U Gem in outburst (Obs. ID 3767), and in two SS Cyg spectra in outburst. In these cases, the excess appears peaked at $\sim 1.01 \pm 0.01$ keV. In U Gem, the centroid energy of the Gaussian component fitted to this excess is compatible with Ne X, Fe XVII and Fe XXI lines. In SS Cyg, this excess is compatible with emission line from either Ca XVIII, Fe XVII, Ni XIX, or Ni XVIII in Obs. ID 648, and Ca XVIII, Ni XIX, and Ne IX in Obs. ID 2307. Other lines, compatible with emission from Mg XI, Mg XII, Si XIII, and Fe XXII were also observed in the *Chandra* spectra, see Table 6. The observation of this broad feature around 1.01 keV in both *XMM-Newton* Epic-pn and HETG/ACIS spectra, and its variability, indicates that this feature is not a systematic effect of our spectral modeling, nor an individual issue of one of the instruments.

It is important to point out that this broad excess likely correspond to a blend of narrow lines emitted by Fe XVII, XIX, XX, and XXI and/or Ne IX-X, and/or Ni XIX ions – which are not very well resolved by the medium energy resolution of the pn camera and HETG/ACIS. Several lines are observed in this soft X-ray energy range by LETG/HRC grating spectrometer (due its resolving power > 1000) (see also, e.g. Mukai et al. 2003; Pandel et al. 2003). For example, in our analysis of the LETG/HRC SS Cyg spectrum, lines at ~ 0.82 keV, ~ 0.92 keV, and ~ 1.0 keV were clearly present.

7. SUMMARY AND CONCLUSIONS

The thermal Comptonization model plus Gaussian components (used to account for the emission lines) can successfully describe the spectra of the nMCVs in our source sample. Though we did not find a perfect fit, in terms of χ^2 statistics, to the *XMM-Newton* spectra of VW Hyi and U Gem, both the *Chandra* HETG/ACIS and *RXTE* PCA spectra of the later source were satisfactory fitted by our Comptonization model. It is likely that the presence of many lines, besides the iron complex, in the *XMM-Newton* spectra of VW Hyi and U Gem worsened the fit quality.

The *XMM-Newton* and *Chandra* spectra show a similar range of physical parameters. However, the *RXTE* spectra, due to the broader spectral energy range, provided a better description of the Comptonization effect and determination of the physical parameters. We found that two Comptonization components are necessary to successfully fit the simultaneous 0.4–150 keV *Chandra/RXTE* spectra of SS Cyg in quiescence, and two 2.5–25 keV *RXTE* spectra of SS Cyg in outburst. In this case, the best-fits are found only if the optical depth and the plasma temperature of the Compton cloud are the same for these two components. As a results we found the only one photon index $\Gamma \sim 1.8$ is capable to describe the total spectra of all analyzed nMCVs.

Two blackbody components of seed photons are characterized by their color temperature (kT_{s1} and kT_{s2}). In our interpretation, the seed photon component showing lowest temperatures ($kT_{s1} \sim 0.1\text{--}0.2$ keV) is presumably coming from the inner part of the accretion disk or outer part of the

TL, while the second and transient component related to kT_{s2} is coming from a more internal part of the system, closer to the WD surface. We rather think that these temperatures are related to the innermost part of the corona (TL) than they are associated with a WD surface, otherwise a value of $kT_{s2} \sim 0.6\text{--}0.8$ keV could exceed the appropriate temperature limit for the existence of bounded atmospheres on WDs.

The seed photons are up scattered by hot electrons in the TL characterized by a single electron temperature kT_e (in the 5–48 keV range), and located between the disk and the WD surface. The TL optical depth changes in the wide range $1 \lesssim \tau_0 \lesssim 5$.

When we compared the physical parameters between different sources in different states, we did not find any correlation of Γ (or $\alpha = \Gamma - 1$) with the plasma temperature kT_e (see Fig 9), nor a clear correlation of physical parameters with the source stage. However, the *RXTE* observations of SS Cyg show a clear change of the electron temperature in the Compton cloud (or TL) when the source is found in different states: it is higher in quiescence, 33_{-3}^{+3} keV; it decreases to 25_{-1}^{+1} keV at the initial stage of the optical outburst; and reaches $\sim 5.5_{-0.3}^{+0.4}$ keV during a rise of the outburst. This decrease in the electron temperature can explain the suppression of hard X-rays ($\gtrsim 25$ keV) during outburst in SS Cyg. Therefore, the dependence of the physical parameters with the source stages may depend on the source.

Finally, we conclude that our two thermal Comptonization component model using a single thermal plasma temperature and optical depth plus Gaussian components can describe the 0.4–150 keV spectra of nmCVs, in both quiescence and outburst states, without evoking more than one optically thin plasma temperature or cooling flow models.

Moreover, we develop the radiative transfer model which rigorously demonstrates and explains our main observational result, using the first principal arguments, that the photon indices, Γ in WDs should be around 1.8 (see Fig. 9).

ACKNOWLEDGMENTS

T.M. acknowledges the financial support given by the Erasmus Mundus Joint Doctorate Program by Grants Number 2013-1471 from the agency EACEA of the European Commission, and the INAF/OAS Bologna. T.M. acknowledges the support given by the National Program on Key Research and Development Project (Grants No. 2016YFA0400803) and the NSFC (11622326 and U1838103). T.M. also thanks the High Energy Astrophysics group of the Physics Dept. of the University of Ferrara, INAF/OAS Bologna and Wuhan University for the warm hospitality and support. L.T. appreciates the interest and support of his colleagues from the Physical Institute of the Russian Academy of Science (FIAN). M.O. acknowledges support from the Italian Space Agency under grant ASI-INAF 2017-14-H.0. The authors are grateful to the anonymous referee for the constructive suggestions.

REFERENCES

- Barlow, R. 1989, *Statistics. A guide to the use of statistical methods in the physical sciences* (The Manchester Physics Series, New York: Wiley, 1989)
- Baskill, D. S., Wheatley, P. J., & Osborne, J. P. 2005, *MNRAS*, 357, 626

- Belloni, T., Verbunt, F., Beuermann, K., Bunk, W., Izzo, C., Kley, W., Pietsch, W., Ritter, H., Thomas, H. C., & Voges, W. 1991, *A&A*, 246, L44
- Byckling, K., Mukai, K., Thorstensen, J. R., & Osborne, J. P. 2010, *MNRAS*, 408, 2298
- D'Aí, A., Życki, P., Di Salvo, T., Iaria, R., Lavagetto, G., & Robba, N. R. 2007, *ApJ*, 667, 411
- D'Amico, F., Heindl, W. A., Rothschild, R. E., & Gruber, D. E. 2001, *ApJL*, 547, L147
- Di Salvo, T., Goldoni, P., Stella, L., van der Klis, M., Bazzano, A., Burderi, L., Farinelli, R., Frontera, F., Israel, G. L., Méndez, M., Mirabel, I. F., Robba, N. R., Sizun, P., Ubertini, P., & Lewin, W. H. G. 2006, *ApJL*, 649, L91
- Done, C., & Osborne, J. P. 1997, *MNRAS*, 288, 649
- Farinelli, R., & Titarchuk, L. 2011, *A&A*, 525, A102+
- Farinelli, R., Titarchuk, L., Paizis, A., & Frontera, F. 2008, *ApJ*, 680, 602
- Friend, M. T., Martin, J. S., Connon-Smith, R., & Jones, D. H. P. 1990, *MNRAS*, 246, 654
- George, I. M., & Fabian, A. C. 1991, *MNRAS*, 249, 352
- Godon, P., & Sion, E. M. 2005, *MNRAS*, 361, 809
- Guainazzi, M. 2016, XMM-SOC-CAL-TN-0018, Xmm-newton calibration technical note, ESA-ESAC, Villafranca del Castillo, Spain
- Güver, T., Uluýazı, C., Özkan, M. T., & Göğüş, E. 2006, *MNRAS*, 372, 450
- Harrison, T. E., Johnson, J. J., McArthur, B. E., Benedict, G. F., Szkody, P., Howell, S. B., & Gelino, D. M. 2004, *AJ*, 127, 460
- Harrison, T. E., McNamara, B. J., Szkody, P., & Gilliland, R. L. 2000, *AJ*, 120, 2649
- Harrison, T. E., McNamara, B. J., Szkody, P., McArthur, B. E., Benedict, G. F., Klemola, A. R., & Gilliland, R. L. 1999, *ApJL*, 515, L93
- Hasenkopf, C. A., & Eracleous, M. 2002, in *Bulletin of the American Astronomical Society*, Vol. 34, American Astronomical Society Meeting Abstracts, 1301
- Hua, X.-M., & Titarchuk, L. 1995, *ApJ*, 449, 188
- Ishida, M., Okada, S., Hayashi, T., Nakamura, R., Terada, Y., Mukai, K., & Hamaguchi, K. 2009, *PASJ*, 61, S77
- Iyer, N., Mukherjee, D., Dewangan, G. C., Bhattacharya, D., & Seetha, S. 2015, *MNRAS*, 454, 741
- Lewin, W. H. G., & van der Klis, M. 2006, *Compact Stellar X-ray Sources*, 39 (Cambridge University Press)
- Liedahl, D. A., Osterheld, A. L., & Goldstein, W. H. 1995, *ApJL*, 438, L115
- Long, K. S., Mauche, C. W., Raymond, J. C., Szkody, P., & Mattei, J. A. 1996, *ApJ*, 469, 841
- Maiolino, T., D'Amico, F., & Braga, J. 2013, *A&A*, 551, L2
- Maiolino, T., Laurent, P., Titarchuk, L., Orlandini, M., & Frontera, F. 2019, *A&A*, 625, A8
- Mason, K. O., Cordova, F. A., Watson, M. G., & King, A. R. 1988, *MNRAS*, 232, 779
- Mauche, C. W., & Raymond, J. C. 2000, *ApJ*, 541, 924
- Mauche, C. W., & Robinson, E. L. 2001, *ApJ*, 562, 508
- Mewe, R., Lemen, J. R., & van den Oord, G. H. J. 1986, *A&AS*, 65, 511
- Montanari, E., Titarchuk, L., & Frontera, F. 2009, *ApJ*, 692, 1597
- Mukai, K. 2017, *PASP*, 129, 062001
- Mukai, K., Kinkhabwala, A., Peterson, J. R., Kahn, S. M., & Paerels, F. 2003, *ApJL*, 586, L77
- Mushotzky, R. F., & Szymkowiak, A. E. 1988, in *NATO Advanced Science Institutes (ASI) Series C*, Vol. 229, NATO Advanced Science Institutes (ASI) Series C, ed. A. C. Fabian, 53–62
- Nakaniwa, N., Hayashi, T., Takeo, M., & Ishida, M. 2019, *MNRAS*, 488, 5104
- Okada, S., Nakamura, R., & Ishida, M. 2008, *ApJ*, 680, 695
- Orlandini, M., Frontera, F., Masetti, N., Sguera, V., & Sidoli, L. 2012, *ApJ*, 748, 86
- Pandel, D., Córdoba, F. A., & Howell, S. B. 2003, *MNRAS*, 346, 1231
- Pandel, D., Córdoba, F. A., Mason, K. O., & Priedhorsky, W. C. 2005, *ApJ*, 626, 396
- Patterson, J., & Raymond, J. C. 1985a, *ApJ*, 292, 550
- . 1985b, *ApJ*, 292, 535
- Polidan, R. S., Mauche, C. W., & Wade, R. A. 1990, *ApJ*, 356, 211
- Press, W. H., Teukolsky, S. A. and Vetterling, W. T., & Flannery, B. P. 1992, *Numerical recipes in C. The art of scientific computing* (Cambridge: University Press, —c1992, 2nd ed.)

- Pringle, J. E., & Savonije, G. J. 1979, *MNRAS*, 187, 777
- Rana, V. R., Singh, K. P., Schlegel, E. M., & Barrett, P. E. 2006, *ApJ*, 642, 1042
- Raymond, J. C., & Smith, B. W. 1977, *ApJS*, 35, 419
- Ritter, H., & Kolb, U. 2003, *VizieR Online Data Catalog*, 5113
- Rothschild, R. E., Blanco, P. R., Gruber, D. E., Heindl, W. A., MacDonald, D. R., Marsden, D. C., Pelling, M. R., Wayne, L. R., & Hink, P. L. 1998, *ApJ*, 496, 538
- Rybicki, G. B., & Lightman, A. P. 1979, *Radiative Processes in Astrophysics* (New York, Wiley-Interscience, 1979. 393 p.)
- Schoembs, R., & Vogt, N. 1981, *A&A*, 97, 185
- Shafter, A. W., & Harkness, R. P. 1986, *AJ*, 92, 658
- Sion, E. M., Cheng, F. H., Sparks, W. M., Szkody, P., Huang, M., & Hubeny, I. 1997, *ApJL*, 480, L17
- Sunyaev, R. A., & Titarchuk, L. G. 1980, *A&A*, 86, 121 (ST80)
- . 1985, *A&A*, 143, 374
- Szkody, P., Long, K. S., Sion, E. M., & Raymond, J. C. 1996, *ApJ*, 469, 834
- Szkody, P., Nishikida, K., Raymond, J. C., Seth, A., Hoard, D. W., Long, K. S., & Sion, E. M. 2002, *ApJ*, 574, 942
- Titarchuk, L. 1994, *ApJ*, 434, 570
- Titarchuk, L., & Lyubarskij, Y. 1995, *ApJ*, 450, 876
- Titarchuk, L., Seifina, E., & Shrader, C. 2014, *ApJ*, 789, 98
- van der Woerd, H., & Heise, J. 1987, *MNRAS*, 225, 141
- Warner, B. 1987, *MNRAS*, 227, 23
- . 1995, *Cambridge Astrophysics Series*, 28
- Williams, G. A., King, A. R., & Brooker, J. R. E. 1987, *MNRAS*, 226, 725
- Xu, X.-j., Wang, Q. D., & Li, X.-D. 2016, *ApJ*, 818, 136